International Journal of Heat and Mass Transfer 270 (2026) 129203

Contents lists available at ScienceDirect

International Journal of Heat and Mass Transfer

journal homepage: www.elsevier.com/locate/hmt

Offset dense jets in co-and-counter flow: Experimental and numerical study

Sina Tahmooresi [a,*], Abdolmajid Mohammadian [a], Ioan Nistor [a], Simone Ferrari [b]

[a] Department of Civil Engineering, University of Ottawa, 161 Louis Pasteur, Ottawa, ON K1N 6N5, Canada
[b] Department of Civil Engineering and Architecture, University of Cagliari, Via Università 40, 09124, Cagliari, Italy

ARTICLE INFO

Keywords:
Co-flow
Counter-flow
Confinement
Turbulence
Buoyancy
Jet

ABSTRACT

This study investigates the mixing behavior of turbulent offset dense jets discharged into co- and counter-flowing ambient currents under varying confinement ratios. A comprehensive experimental campaign using planar laser-induced fluorescence (PLIF) was conducted for two densimetric Froude numbers, supported by Reynolds-averaged numerical simulations. The experiments reveal that co-flow produces smoother centerline decay trends and more asymptotic behavior, whereas counter-flow often triggers low-frequency oscillations, enhanced lateral spreading, and delayed decay. Confinement plays a central role: at small confinement ratios, the counter-flow jet forms persistent recirculation zones, suppressing flapping motions and reducing dilution; at larger confinement ratios, counter-flow promotes stronger unsteadiness and faster decay at sufficiently high current Froude number. Proper orthogonal decomposition (POD) was employed to examine the large-scale dynamics and revealed that counter-flow scenarios exhibit pronounced low-frequency flapping behavior, whose strength and spatial extent depend strongly on confinement. Numerical predictions captured the general trajectory and recirculation patterns but consistently over-predicted dilution, especially at higher current Froude number values. The combined results provide new insight into offset jets released into non-stagnant coastal environments.

1. Introduction

Jet flows are generally classified as free or bounded, depending on the proximity of the jet to confining boundaries. A free jet occurs when the surrounding boundaries are sufficiently distant from the jet outlet, allowing the flow to develop without obstruction. In contrast, bounded jets arise when the jet interacts with a nearby parallel surface. Bounded jets can be further categorized into three types based on their interaction with the containment wall: (a) an impinging jet, where the jet is directed perpendicularly toward the boundary (e.g., [1,2]); (b) a wall jet, where the fluid is discharged tangentially along the surface (e.g., [3,4]); and (c) an offset jet, which emerges when a jet discharges into a medium above a horizontal solid boundary, remaining parallel to the jet axis but positioned at a certain offset distance from the wall (e.g., [5–8]).

The flow dynamics of an offset jet are inherently complex and play a critical role in numerous engineering applications. For instance, offset jets significantly influence the performance of burners, boilers, gas turbine combustion chambers, and fuel injection systems, where their behavior dictates mixing efficiency, combustion stability, and heat transfer characteristics [9–11]. From an environmental fluid mechanics perspective, offset jets serve as an effective means of discharge [12,13]. Although inclined jets (e.g., [14–19]) are frequently employed to enhance mixing efficiency in discharge jet flows due to their extended trajectory, the offset discharge of jets remains highly relevant. This preference is primarily driven by practical considerations, including simplified construction, lower implementation costs, and the physical constraints of shallow water environments, where inclined configurations may be less feasible [20–22]. When analyzed in the context of receiving ambient, offset jets can be classified on the basis of the nature of the ambient flow. They may occur in stagnant, co-flow, counter-flow, or cross-flow conditions, depending on whether the jet is discharged into a quiescent or moving ambient environment. The classification is determined by the alignment between the jet and the surrounding flow, where a co-flow scenario arises when the jet moves in the same direction as the background current (e.g., [23,24]), a counter-flow occurs when the jet opposes the ambient flow (e.g., [25,26]), and a cross-flow condition refers to cases where the jet interacts with an ambient flow that is perpendicular to its axis, (e.g., [27–29]). In shallow estuarine or coastal regions, the periodic reversal or oscillation of tidal currents effectively creates alternating co-flow and counter-flow conditions that influence jet mixing and entrainment [30–33].

In addition to the aforementioned classification, the density difference between the jet and the surrounding ambient fluid also plays

* Corresponding author.
E-mail address: stahm017@uottawa.ca (S. Tahmooresi).

https://doi.org/10.1016/j.ijheatmasstransfer.2026.129203
Received 19 February 2026; Received in revised form 6 April 2026; Accepted 22 June 2026

a crucial role in shaping the evolutionary behavior of the jet. This influence is primarily governed by buoyancy effects, which categorize jets into buoyant and non-buoyant types. Buoyant jets, in particular, are further classified according to the relative density difference, commonly referred to as positively buoyant (e.g., [34]), negatively buoyant (e.g., [35]), or dense jets (e.g., [36–38]), depending on whether the jet fluid is lighter or heavier than the ambient medium. In a negatively buoyant jet, the buoyancy opposes the momentum [35,39]. In a dense jet, however, it suffices for the jet to have a heavier density, compared to the receiving ambient, no matter what direction has the buoyancy force against the momentum (e.g., offset and inclined dense jets).

The offset ratio H_0/D defined as the ratio of the vertical distance between the jet exit center and the adjacent wall H_0 to the nozzle diameter D, plays a significant role in governing the dynamics and mixing behavior of round turbulent offset jets. As the offset ratio increases, the flow exhibits characteristics more akin to a free jet, whereas a decrease in the offset ratio results in behavior that increasingly resembles a wall jet [4,5,13]. Furthermore, when a dense offset jet is discharged into a non-stagnant ambient environment, the flow dynamics become even more complex due to the additional influence of the background current. The present study aims to highlight the interplay between the offset ratio, density difference, and ambient flow conditions in shaping the behavior of round offset dense jets.

Early studies on offset jets have explored various critical aspects, including reattachment length, Reynolds number effects, wall static pressure distribution, mean velocity fields, and turbulence intensities (e.g., [40–42]). Early investigations predominantly focused on two-dimensional (2D) plane offset jets, as seen in studies such as [43–47]. These works provided experimental data on static pressure distributions, mean velocity profiles, and turbulence statistics, using techniques like Pitot tubes, hot-wire anemometry, laser Doppler anemometry (LDA), and particle image velocimetry (PIV) to characterize jet behavior and interactions with the wall. There are several studies that report on the heat transfer characteristics of offset jets (e.g., [48–50]).

Leaving the focus on three-dimensional (3D) offset jets, in an early study, [51], and more recently [4,52], investigated 3D cases. In their comprehensive study, [4] investigated the influence of the offset ratio and Reynolds number on the structure of turbulent offset jets. Using PIV, their findings revealed that in the early stages of flow development, both the Reynolds number and the offset ratio significantly impact the decay of the maximum mean velocity and the growth of the shear layer. However, at larger downstream distances, the decay and spread rates become nearly independent of the offset ratio. Furthermore, as previously reported by [53], the lateral and vertical profiles of the streamwise mean velocity in offset jets exhibit self-similarity and appear independent of orifice geometry. However, the Reynolds stresses do not follow the same self-similar trend and may be influenced by the initial conditions [4].

In recent years, a limited number of experimental studies have addressed the behavior of turbulent offset dense jets with confinement effects. In contrast, the literature features a more extensive body of research focused on horizontal positively buoyant jets, particularly under conditions of bottom and surface confinement (e.g., [54–60]). Notably, the two-component studies by [6,20], the investigation by [61], and the four-component studies by [62–65] directly address the topic of turbulent horizontal dense jets. These studies employ simultaneous PIV and planar laser induced fluorescence (PLIF) techniques, and they were conducted under stagnant condition. Recently, [66] conducted an experimental investigation of offset jets under both free and confined configurations, exploring a range of offset ratios from $H_0/D = 3$ to 20. Their study provided data on the mean and turbulent characteristics of the scalar concentration field over large downstream distances. For the case with $H_0/D = 3$, the self-similarity of the mean concentration profiles was confirmed. However, the root-mean-square (RMS) of concentration fluctuations did not exhibit self-similarity and continued to evolve down to $70 \times D$ downstream from the impingement point. In the current study, scenarios were conducted in non-stagnant conditions.

The dynamic of the background ambient to which the jet is released into add to the complexity, as mentioned before. With regard to jet in co-flow scenarios, there are numerous studies in the past. The self-similarity of the mean velocity and concentration, as an important subject, were investigated from decades ago (e.g., [67–70]). Among these studies, there were reports on the Reynolds stresses not showing the self-similarity [67,68], an observation that was further confirmed by [70]. To predict the spreading and mixing characteristics of an axisymmetric turbulent jet in a co-flow, [71] conducted experimental scenarios using LIF and LDA to present a Lagrangian-based integral model. Inclined dense jets in co-flow were investigated in [23]. They investigated the mixing and transport of the resulting density current after the 60° dense jet impinges on a horizontal bottom boundary, focusing on the influence of cross-flow Froude number, $U_r F$, with $U_r = \frac{U_a}{U_j}$ as the ambient to jet velocity ratio and F (Eq. (2)) as the densimetric Froude number on flow regimes including bifurcation and upstream intrusion. 45° inclined dense jets in co-flow were experimentally investigated using LIF in [72]. Authors found that the jets exhibited two mixing regimes. A dense-jet-dominated regime at low co-flow conditions and a co-flow-dominated regime at higher current speeds. [73] conducted a related study on 45° inclined dense jets in co- and counter-flow conditions over a wider range of velocity ratios, with $U_r F$ spanning from -3 to 3. Their results indicated that $U_R F = 1$ represents a critical threshold separating jet-dominated cases from those dominated by the ambient flow. [8] performed an experimental and numerical (using Reynolds Stress Models) study on offset dense jets in stagnant and co-flow conditions. Scenarios were consisting of different velocity ratios in a broad range of R $(= U_j/U_a)$, $R = 1$, and $R = \infty$, and $H_0/D = 5.3$ and 7.8, as varying confinement ratios. A recent study by [74] investigated inclined dense jets in more realistic coastal environments by incorporating wave-induced motions using both experimental data and CFD modeling. Their results showed that wave action introduces oscillatory behavior near the jet source, enhancing entrainment and significantly increasing dilution compared to stagnant conditions, while also modifying the jet trajectory and spreading characteristics. Furthermore, the interaction between wave-induced shear and jet momentum was found to alter the flow geometry and accelerate pollutant dispersion.

More recently, [75] experimentally investigated how varying levels of background turbulence in a co-flow affect a turbulent non-buoyant jet's behavior regarding velocity, spread, and mixing at different Reynolds numbers. [13] studied the dynamics of round turbulent offset jets with offset ratios of 2, 4, and 6, released into both a quiescent environment and a co-flowing stream. The researchers used an acoustic Doppler velocimeter to measure the velocity field in a water flume. The results indicate that the spreading and decay rates decrease in the presence of co-flow, indicating that the external flow restricts the jet's growth and development. This effect is more pronounced at smaller offset ratios.

Although free turbulent round jets are among the most extensively studied flows, round jets in counter-flow configurations have received comparatively limited attention in the literature [76]. In a counter-flow jet configuration, the jet is discharged directly against an opposing uniform stream. The jet-to-counter-flow velocity ratio, defined as $\alpha = \frac{U_j}{U_a} \equiv 1/U_r$ governs the stability of the resulting flow. When $\alpha < 1.4$, the interaction gives rise to periodic, symmetric vortex shedding [77]. However, when this threshold is exceeded – particularly at high Reynolds numbers – the flow transitions into a chaotic and seemingly unstable regime [76]. [76] conducted a literature review on jets in counter-flow configurations, identifying key parameters that influence jet behavior. Among the most significant factors are the jet penetration length, boundary conditions and confinement, and the large-scale dynamics of the flow. The jet penetration length x_p defined as the distance from the jet exit to the stagnation point where the jet momentum is balanced by the opposing flow, has been classically described by [78] through the relation $x_p/D = k \cdot \alpha$, where k is an empirical constant. Subsequent studies by [26,79–82] extended this analysis by exploring both the streamwise and spanwise (radial) penetration behaviors of non-buoyant jets in counter-flow conditions. [83] experimentally investigated the turbulent structure of round jets in counter-flow using acoustic Doppler velocimetry (ADV) to obtain time-resolved velocity measurements of the flow field. The study showed that counter-flow conditions accelerate axial velocity decay while reducing entrainment mechanisms. [84] performed a numerical parametric investigation of turbulent round jets in counter-flow using a Reynolds Stress Model to assess the influence of velocity ratio, Reynolds number, and jet inclination. Their results confirmed a linear relationship between penetration length and velocity ratio within low momentum flux regimes, while showing that Reynolds number effects become negligible beyond critical thresholds.

The role of confinement in influencing jet penetration in counter-flow was further highlighted in the context of wall jets, where studies such as [85,86] demonstrated that confinement leads to increased penetration lengths compared to unconfined counterparts. More recently, [87] conducted experimental investigations into the turbulent statistics of both free and offset jets in counter-flow environments. Their findings indicated that the offset and free jets exhibited similar global behavior, yet when compared to a free jet discharging into a quiescent ambient, both configurations showed elevated axial and radial turbulence intensities, which contributed to enhanced dilution.

Another important phenomenon observed in counter-flow jets is the presence of low-frequency oscillatory behavior. Using two-dimensional Proper orthogonal decomposition (POD), [88] identified that, at $\alpha = 3.4$, the jet exhibited two dominant modes as axial and radial. This was later expanded upon by [89], who revealed that what appeared as two-dimensional flapping behavior was, in fact, three-dimensional in nature, pointing to the complex spatial dynamics of jets in counter-flow.

The present study investigates the mixing behavior of offset dense jets under both co-flow and counter-flow conditions using PLIF technique. As highlighted in the preceding literature review, previous investigations have largely focused on offset jets in stagnant environments (whether buoyant, dense, or non-buoyant) or on non-buoyant and positively buoyant jets exposed to co-flow or counter-flow, often with or without confinement. This study aims, for the first time, to bridge that gap by examining how the superposition of offset geometry and ambient flow directionality influences the dilution of discharged mass as dense jets in non-stagnant environments that resembles the coastal waters conditions. This novel experimental program was further supported by non-dimensional numerical simulation approach in order to represent a more detailed analysis of the mixing mechanisms.

The rest of the paper is organized as follows. Section 2 describes the experimental methodology. Section 3 presents the numerical modeling approach. Section 4 discusses the main results, with primary emphasis on mixing characteristics and bulk flow parameters. Sections 5 and 6 are devoted to a detailed investigation of the counter-flow instability and POD analysis, respectively. Section 7 evaluates the performance of the numerical model and discusses the main sources of experimental and numerical uncertainties. Finally, Section 8 summarizes the main findings and conclusions of the study. Additional material is provided in the appendices, and supplementary material accompanies this paper.

2. Experimental method

2.1. Experimental scenarios

A schematic representation of an offset dense jet in counter-flow configurations is provided in Fig. 1. The jet is discharged horizontally, parallel to the bottom boundary, with its behavior governed by the interplay of momentum and buoyancy forces. These forces are characterized by two non-dimensional parameters: the jet Reynolds number, defined as

$$Re = \frac{U_j}{\nu D} \tag{1}$$

and the densimetric Froude number, given by

$$F = \frac{U_j}{\sqrt{g' D}} \tag{2}$$

where U_j is the jet exit velocity, D is the nozzle diameter, and ν is the kinematic viscosity of water. The term g' represents the reduced gravity, calculated as

$$g' = g\frac{\rho_j - \rho_a}{\rho_a} \tag{3}$$

where ρ_j and ρ_a are the densities of the jet and ambient fluid ($\rho_j > \rho_a$), respectively. The offset height, the vertical distance from the bottom boundary to the centerline of the jet nozzle, is denoted by H_0, as seen in Fig. 1. The coordinate system used in this study is defined such that the streamwise direction aligns with the x-axis, the vertical (gravitational) direction corresponds to the y-axis, and the spanwise direction is along the z-axis.

Applying dimensional analysis to offset jets in a flowing ambient, it becomes evident that the interaction between the ambient current and the turbulent dense jet influences the jet dynamics through a combined non-dimensional parameter denoted as U_rF. Here, the velocity ratio is defined as $U_r = U_a/U_j = 1/\alpha$. Therefore:

$$U_rF = \frac{U_a}{\sqrt{g' D}} \tag{4}$$

where U_j disappear and U_rF can be considered as current Froude number [23]. In addition to the interaction between the ambient and jet momentum and buoyancy, the offset distance can also be incorporated into the analysis through dimensional parameterization, commonly expressed as the offset ratio H_0/D.

To design the experimental scenarios, the key non-dimensional parameters, Reynolds number Re, Froude number F, current Froude number U_rF, and offset ratio H_0/D, must be defined. Prior studies provide guidance for selecting U_rF values. For vertical and 60° inclined dense jets in cross-flow, [90] reported $1.35 < U_rF < 5$, while [91] extended this range up to $U_rF = 8$ using high current speeds. [92] explored $0 < U_rF < 10.6$ and distinguished weak cross-flow for $U_rF < 0.7$ and strong cross-flow for $U_rF > 0.7$ based on changes in jet trajectory. According to [27], $U_rF > 1$ represents a fairly strong cross-flow, and at $U_rF = 2$, the jet fails to reach the bottom boundary. In co-flowing conditions, [23] identified $U_rF = 0.8$ as the threshold beyond which upstream intrusion ceases, classifying it as a strong co-flow regime. Based on these findings, the present study selects $U_rF = 0.25, 0.5, 1, 1.25$ to span both weak and fairly strong regimes. The selected values of the U_rF are also consistent with field-scale conditions reported in the literature. For instance, [93] considered a range of $U_rF = 0.2$–1.6, corresponding to ambient velocities representative of coastal discharge environments and real outfall systems, as previously documented by [94]. For counter-flow scenarios, [77] reported a critical velocity ratio $\alpha \simeq 1.4$, above which low-frequency instabilities arise in round jets due to the opposing uniform ambient flow. In the case of a dense jet, however, this parameter is more appropriately expressed through U_rF, since buoyancy (via the densimetric Froude number F) alters the jet trajectory and can suppress or delay the onset of such instabilities. This behavior was clearly demonstrated in [95], who examined positively buoyant jets over a range of densiemetric Froude numbers $F = 2.5, 5, 7.5, 18$ and jet-to-counter-flow velocity ratios $\alpha = 2.5, 5, 7.5, 18$. In the present experiments, cases with $U_rF \geq 1$ consistently exhibited global, low-frequency oscillatory behavior, as discussed in detail in Section 5. Consequently, the selected range of current Froude numbers U_rF is expected to cover a range of counter-flow mixing and instability patterns.

The Reynolds number was fixed at $Re = 2400$, representing a value above minimum threshold of $Re \approx 2000$ required to ensure the transition to turbulence immediately downstream of the nozzle exit [96,97]. The selected Reynolds number ensures fully turbulent

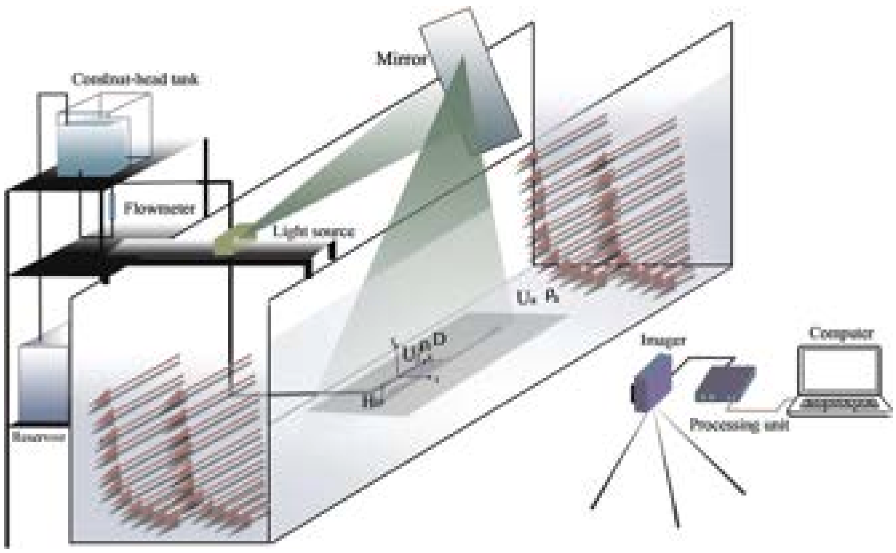

Fig. 1. Schematic view of an offset dense jet in flowing current (counter-flow).

Table 1
Summary of experimental scenarios.

H_0/D	F	U_rF	Flow direction	Re	Total no. of scenarios
2.5	15	0.25, 0.5, 1, 1.25	Co-flow/Counter-flow	2400	8
2.5	30	0.25, 0.5, 1, 1.25	Co-flow/Counter-flow	2400	8
5	15	0.25, 0.5, 1, 1.25	Co-flow/Counter-flow	2400	8
5	30	0.25, 0.5, 1, 1.25	Co-flow/Counter-flow	2400	8
10	15	0.25, 0.5, 1, 1.25	Co-flow/Counter-flow	2400	8
10	30	0.25, 0.5, 1, 1.25	Co-flow/Counter-flow	2400	8

conditions while maintaining relatively low discharge rates. This was particularly important for the present study, which involved an extensive experimental program comprising 48 scenarios, as it allowed the total volume of saline solution required to be minimized without compromising the turbulent mixing behavior.

For the densimetric Froude number, two values were selected: $F =$ 15 and 30. These choices maintain a moderate density difference of $\frac{\Delta\rho}{\rho_a}(\%) = 1.17$ and 0.29, respectively, which lie within the acceptable range for dense jet discharges (e.g., [93,98–101]). Additionally, higher Froude numbers help elongate the initial trajectory, minimizing the proximity of the jet to the nozzle exit and enhancing flow development.

For the offset ratio parameter H_0/D, three values were selected: $H_0/D = 2.5$, 5, and 10. [66] demonstrated that for $H_0/D > 10$, the effects of confinement become negligible. Therefore, the chosen values were intentionally kept below this threshold. Considering four U_rF values, two Froude numbers $F = 15$ and 30, and both co-flow and counter-flow configurations, a total of 48 co-and-counter flow experimental scenarios were designed. These scenarios are summarized in Table 1.

2.2. Experimental setup

The experimental campaign was carried out at the Hydraulics Laboratory of the University of Cagliari, Italy. The setup featured a glass flume, measuring 8 m in length, 0.4 m in width, and 0.5 m in depth, which facilitated clear visual access to the flow. The potential influence of side-wall confinement was minimized by the relatively large flume width compared with the nozzle diameter. In the present setup, $B/D \approx 66.7$ (with $D = 6$ mm and B as the nozzle diameter and the flume width, respectively), corresponding to a lateral distance of approximately $33D$ from the jet centerline to each side wall. Based on established jet spreading relations (e.g., [96]), the characteristic concentration edge ($C/C_m = 1/e$) grows approximately as $b_c \approx 0.135x$, implying that the lateral extent of the jet remains well within the central region of the flume over the measurement domain. The observed concentration fields remained symmetric about the centerline, with no indication of lateral distortion or interaction with the side boundaries. A reservoir tank, situated adjacent to the flume, provided the water supply. The flow rate entering the flume was controlled via a ball valve installed near the upstream tank, while the flow head was adjusted using a movable weir positioned at the downstream end. The nozzle was centrally positioned along the width of the flume. To accommodate both co-flow and counter-flow scenarios, two configurations were constructed. In the co-flow setup, the final streamwise segment of the nozzle was reversed, enabling the jet to discharge in the same direction as the ambient flow (see Fig. 1). The nozzle is axisymmetric, and therefore no directional bias in the exit conditions is expected. The observed jet structure was consistent with that of a well-developed turbulent round jet, exhibiting a top-hat-like core in the near field and Gaussian distribution downstream, indicating that the exit flow characteristics were not affected by the configuration. The scalar profiles near the end of the jet core ($x^* = 6$) are presented in Section 4.3. The Froude numbers were deliberately chosen high enough to ensure that any disturbance generated by the spanwise extension of the pipe would not interfere with the jet's development in either flow condition. A constant-head tank was positioned elevated above the nozzle to ensure a steady and consistent flow rate at the nozzle exit. By maintaining a constant Reynolds number throughout the experiments, flow rate variability was minimized, thereby reducing experimental uncertainty. This setup also served to isolate the effects of Reynolds number, allowing the results to reflect changes due solely to other governing parameters. The flow rate at the nozzle was measured using an Omega variable area flow meter, which operates based on the principles of buoyancy and flow displacement. Additionally, two solenoid valves were employed: one dedicated to fixing and maintaining the flow rate, and the other used for controlling the initiation and termination of the flow during the experiments.

Control of the ambient velocity U_a for each scenario was achieved by regulating the head over a rectangular weir (Eq. (22)) installed at the downstream end of the flume, well away from the nozzle location. Prior to each experiment, the head over the weir was adjusted to set the desired flow rate. This procedure, together with the jet flow-rate readings obtained from a variable-area flow meter to provide for jet velocity U_j, constituted the primary sources of uncertainty associated with the imposed jet and ambient flow rate. The uncertainties and sources of experimental error associated with the measurements are discussed in more detail in Section 7.

2.3. Flow visualization

The PLIF technique was utilized to capture the two-dimensional concentration distribution within the jet flow. To quantify the concentration field, TiO_2 was utilized as a scattering tracer. The total mass of TiO_2 added to the source tank was less than 5 g, maintaining an initial concentration ($C_0 \approx 0.1$–0.25 g/L) well within the linear optical regime for TiO_2 nanoparticles [102]. At these dilute concentrations, the system operates in the independent scattering regime, where the total scattered light intensity recorded by the camera (gray-scale values) is directly proportional to the number of nanoparticles in the measurement volume. This approach ensures that secondary scattering and extinction effects (i.e., attenuation of the laser sheet) are negligible, which would otherwise introduce non-linearity in denser suspensions. Furthermore, unlike fluorescent dyes such as Rhodamine 6G, TiO_2 is a physically stable mineral that does not exhibit photobleaching or thermal degradation. Consequently, the normalized intensity $I/I_{\max}$ provides a robust and linear proxy for the non-dimensional concentration C/C_0 across all experimental scenarios. Moreover, using the light intensity at the nozzle exit as the reference value to normalize the local concentration, a concentration reduction is measured rather than the concentration. For this reason, no direct calibration of PLIF values against known salt concentrations was needed [29,103,104].

A diode-pumped solid-state (DPSS) green laser with an output of 5 W and a wavelength of 532 nm was used to illuminate the dye. The resulting light was captured by a high-speed CCD camera (Mikrotron EoSens 4CXP CoaXPress). The camera featured a resolution of 2336 × 1728 pixels and recorded images at a Mono 8-bit grayscale depth, providing 256 levels from black to white. An exposure time of $1/2000$ s was used, and image acquisition was conducted continuously. Prior to each recording sequence, one hundred background images were acquired, averaged during post-processing, and subsequently subtracted from every recorded frame. All abnormal luminosity regions (caused by the nozzle, bubbles, etc.) were removed via the background image subtraction, which also removes possible non-uniformity in the light distribution.

For each experimental scenario, over 5000 images were captured at an acquisition frequency of 25 Hz to ensure a statistically reliable time-averaged scalar field. In the counter-flow configurations, this high frame count was particularly crucial for capturing the unsteady dynamics associated with the flapping behavior of the jet. These dynamic features and their implications are discussed in Section 5.

3. Numerical method

Numerical simulations were conducted to replicate and compare each experimental scenario with its corresponding computational model. Given the large number of test cases, the Reynolds-Averaged Navier–Stokes (RANS) approach was chosen as the preferred numerical method.

3.1. RANS equations

The conservation of mass and momentum equations, commonly known as the Navier–Stokes (NS) equations, for incompressible fluid flow can be expressed as:

$$\nabla \cdot \boldsymbol{u} = 0 \tag{5}$$

$$\frac{\partial \boldsymbol{u}}{\partial t} + \boldsymbol{u} \cdot \nabla \boldsymbol{u} = -\frac{1}{\rho}\nabla p + \nu \nabla^2 \boldsymbol{u} + \boldsymbol{g} \tag{6}$$

where $\boldsymbol{u}$ is the velocity vector, t is time, ρ is the fluid density, p is pressure, ν is the kinematic viscosity, and $\boldsymbol{g}$ is the gravitational acceleration vector representing the body source term.

The transport equation for a scalar C can be written as:

$$\frac{\partial C}{\partial t} + \boldsymbol{u} \cdot \nabla C = D_m \nabla^2 C \tag{7}$$

where D_m is the mass diffusivity.

To model turbulent flows using *Reynolds decomposition*, an instantaneous variable Φ (velocity, pressure, concentration, etc.) is expressed as the sum of the average or mean value, $\overline{\Phi}$, and fluctuation around that mean, ϕ' [105]:

$$\Phi = \overline{\Phi} + \phi' \tag{8}$$

Applying the *Reynolds decomposition* to the conservation of mass (5), NS (6), and the scalar transport (7) equations, one may derive the RANS equations for momentum and scalar:

$$\frac{\partial \overline{\boldsymbol{u}}}{\partial t} + \overline{\boldsymbol{u}} \cdot \nabla \overline{\boldsymbol{u}} = -\frac{1}{\rho}\nabla \overline{p} + \nu \nabla^2 \overline{\boldsymbol{u}} - \nabla \cdot \overline{u'u'} + \boldsymbol{g} \tag{9}$$

$$\frac{\partial \overline{C}}{\partial t} + \overline{\boldsymbol{u}} \cdot \nabla \overline{C} = D_m \nabla^2 \overline{C} - \nabla \cdot \overline{u'c'} \tag{10}$$

where $\overline{\boldsymbol{u}}$ is the averaged velocity vector, $\overline{p}$ is the averaged pressure, $\overline{C}$ is the averaged scalar (e.g., mass concentration), and $\overline{u'u'}$ and $\overline{u'c'}$ are the Reynolds stress tensor and Reynolds flux vector, respectively.

3.2. Non-dimensional equations

From a physical and engineering perspective, formulating the dimensionless form of the governing equations offers significant benefits. It provides immediate insight into the dominant physical phenomena, and consequently, assumptions that can reduce the full model to its most essential components [106]. Non-dimensionalization also becomes particularly valuable when numerous simulations or parametric studies are required. While RANS models already provide a relatively computationally efficient framework, a dimensionless formulation further streamlines the analysis by allowing parameter variations to be represented solely through key non-dimensional groups (e.g., F, Re, $U_r F$, etc.).

To derive the non-dimensional form of the governing equations, a set of appropriate dimensionless variables, denoted by asterisks, are introduced. These are based on characteristic reference scales: length D, inertial time scale D/U_j, reference velocity U_j, and reference scalar C_j. The pressure is scaled by the dynamic pressure ρU_j^2, and the body force by U_j^2/D. Accordingly, the resulting dimensionless variables are defined:

$$\boldsymbol{x}^* = \frac{\boldsymbol{x}}{D}, \boldsymbol{u}^* = \frac{\boldsymbol{u}}{U_j}, t^* = \frac{tu_j}{D}, p^* = \frac{p}{\rho u_j^2}, C^* = \frac{C}{C_j} \tag{11}$$

By substituting these dimensionless variables into Eqs. (6), (7), (9), and (10), the corresponding non-dimensional forms of the NS and scalar transport equations are obtained as follows:

$$\frac{\partial \boldsymbol{u}^*}{\partial t^*} + \boldsymbol{u}^* \cdot \nabla \boldsymbol{u}^* = -\nabla p^* + \frac{1}{Re}\nabla^2 \boldsymbol{u}^* + \frac{1}{F^2}\boldsymbol{g}^* \tag{12}$$

$$\frac{\partial C^*}{\partial t^*} + \boldsymbol{u}^* \cdot \nabla C^* = \frac{1}{ReSc}\nabla^2 C^* \tag{13}$$

$$\frac{\partial \overline{\boldsymbol{u}}^*}{\partial t^*} + \overline{\boldsymbol{u}}^* \cdot \nabla \overline{\boldsymbol{u}}^* = -\nabla \overline{p}^* + \frac{1}{Re}\nabla^2 \overline{\boldsymbol{u}}^* - \nabla \cdot \overline{u'^* u'^*} + \frac{1}{F^2}\boldsymbol{g}^* \tag{14}$$

$$\frac{\partial \overline{C}^*}{\partial t^*} + \overline{\boldsymbol{u}}^* \cdot \nabla \overline{C}^* = \frac{1}{ReSc}\nabla^2 \overline{C}^* - \nabla \cdot \overline{u'^* c'^*} \tag{15}$$

where Sc is molecular Schmidt number and defined as:

$$Sc = \frac{\nu}{D_m} \tag{16}$$

To address the closure problem inherent in the RANS and Reynolds-averaged scalar transport equations, it is required to model the Reynolds stress tensor $\overline{u'u'}$, and Reynolds flux vector $\overline{u'c'}$-with * removed for ease of notation. A variety of turbulence modeling approaches have been developed for this purpose. In the present study, to model the Reynolds stress tensor, the $k-\omega$ $Shear\ Stress\ Transport\ (SST)$ model introduced by [107] was employed. The Shear Stress Transport (SST) formulation combines the advantages of both k–ω [108] and k–ϵ [109] turbulence models. Near the wall, the $k-\omega$ formulation allows for accurate resolution of the boundary layer, making the model suitable for low-Reynolds number flows without the need for additional damping functions. This enables the SST model to be applied all the way down to the wall, including the viscous sub-layer. In the free-stream region, the formulation transitions to a $k-\epsilon$ model behavior, avoiding sensitivity to freestream turbulence levels and improving performance in external flow simulations [107].

Finally, for modeling the Reynolds scalar flux vector, the standard gradient diffusion hypothesis (SGDH) as the most commonly used eddy-viscosity-based approach was employed. SGDH assumes that the turbulent scalar flux is proportional to the gradient of the mean scalar field. Applying SGDH to the Reynolds scalar flux vector in its dimensionless form yields:

$$\overline{u'_i c'} = -\frac{\nu_t}{Sc_t}\frac{\partial C}{\partial x_i} \tag{17}$$

where Sc_t is the turbulent Schmidt number defined as:

$$Sc_t = \frac{\nu_t}{D_t} \tag{18}$$

Here, ν_t represents the eddy viscosity, obtained as part of the solution to the closure problem through the eddy-viscosity model introduced earlier, the $k-\omega$ SST model. D_t is turbulent diffusivity. In this study, the molecular Schmidt number Sc and the turbulent Schmidt number Sc_t were taken as 700 and 0.7, respectively [110,111].

3.3. Numerical setup

3.3.1. Computational domain and grid

All numerical simulations were performed using the non-dimensional form of the governing equations, as introduced in Section 3.2 using OpenFOAM.[1] Accordingly, the computational domain was constructed in non-dimensional units, with all spatial dimensions normalized by the jet nozzle diameter D. This scaling ensures consistency with the dimensionless analysis and facilitates generalized interpretation of the results.

The domain geometry was designed to replicate the essential features of the experimental setup in Section 2.2, with domain lengths extended sufficiently in the streamwise $-200 \le x^* \le 200$, vertical $-H_0/D \le y^* \le 50$, and spanwise $-40 \le z^* \le 40$ directions to eliminate artificial boundary effects in streamwise direction and aligning approximately with dimensions of the flume in vertical and spanwise directions. The nozzle was modeled at an offset height of $H_0/D = 2.5$, 5, or 10, depending on the scenario. Fig. A.1 shows the descritized domain using hexahedral elements for a case with $H_0/D = 10$ for a co-flow scenario. A structured mesh was built in *Gmsh*[2] to discretize the domain, with local refinement near the jet exit, buoyancy direction, and regions of expected high gradients in velocity and scalar fields. To ensure cost-effective mesh independence, a limited number of representative cases were selected from various flow scenarios. These cases were compared based on the jet trajectory geometry, concentration decay, and y^+ which serve as reliable indicators of both vertical and horizontal flow development under different mesh resolutions. The mesh independence study is discussed in Appendix A.1 with more details.

3.3.2. Boundary condition

The boundary conditions were defined as follows: a no-slip condition was applied at the bottom, side walls, and nozzle surfaces, while a zero-gradient condition was imposed at the top boundary. In co-flow scenarios, the downstream boundary served as the zero-gradient, and the upstream boundary was defined as an inlet with a prescribed velocity profile. This configuration was reversed for counter-flow scenarios. At the nozzle inlet, all scenarios were initialized with an estimated fully developed turbulent velocity profile for a circular pipe [6]:

$$u_j = 1.14(1 - 2|r/D|)^{1/7} \tag{19}$$

where r is the radial distance from the pipe centerline, and the line-averaged velocity across the pipe diameter $\overline{u_j} = \int_{-D/2}^{D/2} u(r)dr = 0.997$, approximates unity in the non-dimensional framework. For scalar concentration, zero-gradient conditions were assigned to all boundaries except the jet inlet, where a uniform top-hat profile with unit concentration was prescribed. The numerical simulations leveraged the non-dimensional framework, allowing boundary velocity profiles to be updated based solely on the bottom confinement and the jet-to-ambient velocity ratio. For co-flow scenarios, the upstream boundary condition was prescribed using a power-law turbulent open channel velocity profile as follows [112].

$$u_x = U_{ref}((y + h_0)/h)^{1/7} \tag{20}$$

where u_x denotes the streamwise velocity component, h_0 is the distance from the nozzle center to the bottom (equal to the offset ratio H_0/D in the non-dimensional formulation), and h is the total depth. The reference velocity U_{ref} was estimated as the average flow velocity using

$$U_{ref} = \frac{Q}{Lh} \tag{21}$$

where Q is the discharge over a rectangular weir, calculated by:

$$Q = \frac{2}{3}C_d L\sqrt{2g}H^{3/2} \tag{22}$$

Here, L is the channel width, $C_d = 0.6$ is the discharge coefficient for a sharp-crested weir, and H is the head over the weir. For consistency with the non-dimensional framework, U_{ref} was normalized with the jet inlet velocity. For counter-flow scenarios, the same velocity profile was applied at the downstream boundary, with u_x reversed in direction.

3.3.3. Numerical method and solvers

The numerical simulations were conducted using the open-source finite volume software OpenFOAM. A RANS approach was adopted to model turbulence, specifically using the $k-\omega$ (SST) model for its robustness in capturing near-wall effects and free-stream transitions. The governing equations for momentum and scalar transport were formulated in non-dimensional form, as previously described. These non-dimensional equations were implemented within OpenFOAM by modifying existing solvers (*pimpleFoam*) to reflect the scaled variables and eliminate dependency on physical units. Both the velocity field and the scalar concentration equations were solved using these non-dimensional forms. Spatial discretization was performed using second-order accurate schemes for both convective and diffusive terms. Temporal discretization employed the second-order backward scheme. Second-order temporal and spatial discretization schemes were employed to minimize numerical diffusion and improve the accuracy.

[1] https://www.openfoam.com/

[2] https://gmsh.info/

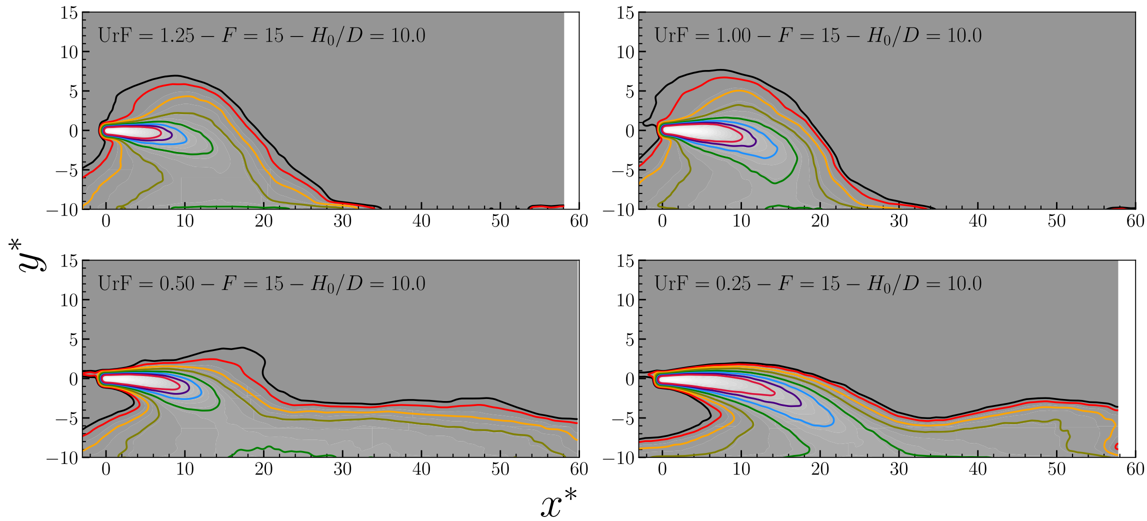

Fig. 2. Counter-flow scenarios for $H_0/D = 10.0$ and $F = 15$. Counter lines represent iso-concentration values of 0.5, 0.4, 0.3, 0.2, 0.1, 0.05, 0.02, and 0.01.

4. Results and discussion

This section begins by examining the concentration fields obtained from both experimental observations and numerical simulations, with a focus on the bulk mixing behavior of the dense jet. The discussion then unfolds to explore the effects of flow configuration (co-flow and counter-flow), confinement through the offset ratio H_0/D, and the influence of the densimetric Froude number F. Finally, the performance of the numerical model is evaluated, with particular attention to its ability to replicate the observed jet dynamics and scalar transport. It is noted, however, that the absence of experimental velocity measurements limits the extent to which a comprehensive validation of the numerical component can be performed.

4.1. General observations

Figs. 2 and 3 present the experimental results for the offset configuration $H_0/D = 10$ and $F = 15$ under counter-flow and co-flow conditions, respectively. Colored iso-concentration lines depict the normalized concentration fields for the different U_rF values at this offset ratio. As U_rF increases, the influence of the ambient co- or counter-flow becomes more evident. In counter-flow cases, the ambient effects first become visible downstream as shown in Fig. 2 for $U_rF = 0.25$ and 0.5. With increasing current Froude number, the jet is pushed back toward the nozzle and its penetration distance decreases. However, because the counter-flow is not very strong, the mean field does not exhibit a full flow reversal. It is also worth noting that for $U_rF = 1.00$ and 1.25 the jet undergoes large-scale oscillations in both the vertical and spanwise directions, marking a three dimensional oscillations, as discussed in Section 5. These oscillation led to an apparent truncation of the mean trajectory at those values of U_rF. In contrast, the co-flow cases exhibit an elongated trajectory as U_rF increases. As indicated by the iso-lines in Fig. 3, larger U_rF values correspond to delayed mixing in the near-nozzle region. The difference between the mixing behaviors of the co-and counter-flow scenarios are discussed in terms of bulk mixing parameters (i.e., centerline decay) and modal analysis in Sections 4.2 and 6, respectively.

The effects of the Froude number on the flow patterns in counter-flow scenarios are shown in Fig. 4, for cases with $H_0/D = 10.0$. Across all U_rF values, the higher Froude number results in elongated trajectories, which reflects the increased dominance of jet momentum over buoyancy, as expected. These differences are most pronounced at lower U_rF, where the $F = 30$ cases exhibit deeper penetration and weaker upstream effects due to confrontation with the counter-flow, compared to their $F = 15$ counterparts. As U_rF increases, the influence of the opposing current becomes more important, and the distinction between the two Froude numbers decreases in the downstream region. At $U_rF = 1.25$, both cases display strong interaction with the counter-flow, though the $F = 30$ scenarios maintain a broader jet footprint and reduced curvature near the nozzle.

Changing the offset ratio further alters the flow pattern and, consequently, the mixing behavior. This is evident in Fig. 5. A decrease in the offset ratio reduces the degree to which the jet is pushed upstream under counter-flow conditions, as well as the severity of its oscillatory motion (as discussed in Section 5). This occurs because the lower offset places the jet closer to the bottom boundary, where confinement suppresses vertical motion. The out-of-plane mixing is also influenced by this confinement, shifting farther downstream compared with the cases with a larger offset ratio. Experimental videos illustrating the flow dynamics discussed in this study are provided as supplementary material.

In the following sections, the numerical model results are included in several figures. However, the detailed evaluation of the numerical performance is provided separately in Section 7.

4.2. Mixing

All numerical and experimental scenarios results on the centerline concentration decay are categorized based on their confinement ratios H_0/D in Figs. 6 and 7 for $H_0/D = 2.5$, and Figs. 8 and 9 for $H_0/D = 5.0$, and Figs. 10 and 11 for $H_0/D = 10.0$. One should note that, in all figures throughout the following sections, CN and CO refer to counter-flow and co-flow conditions, respectively. For a clearer separation between cases, the flow regimes are divided into regions before and after the normalized distance reaches the value of F. The length scale x^*/F can be used to approximate the distance over which the jet momentum remains dominant. Beyond this point, ambient effects such as buoyancy or the background current become increasingly important. [113]. The use of x^*/F is mathematically equivalent to scaling the downstream distance by the jet-to-plume length scale l_M. For a circular dense jet, l_M is analytically shown to be proportional to $D \cdot F$ [114,115]. Therefore, the normalized coordinate x^*/F represents the physical ratio x/l_M (within a constant factor of ≈ 0.94). Across all three confinement ratios, the cases with $F = 30$ generally lie below their $F = 15$ counterparts in the initial region where $x/D \leq F$. Two scenarios with $F = 30$, namely $U_rF = 1.00$ at $H_0/D = 2.5$ in counter-flow and $U_rF = 1.25$ at $H_0/D = 10.0$ in co-flow, were excluded from the figures due to experimental issues that resulted in reduced data quality and lack of

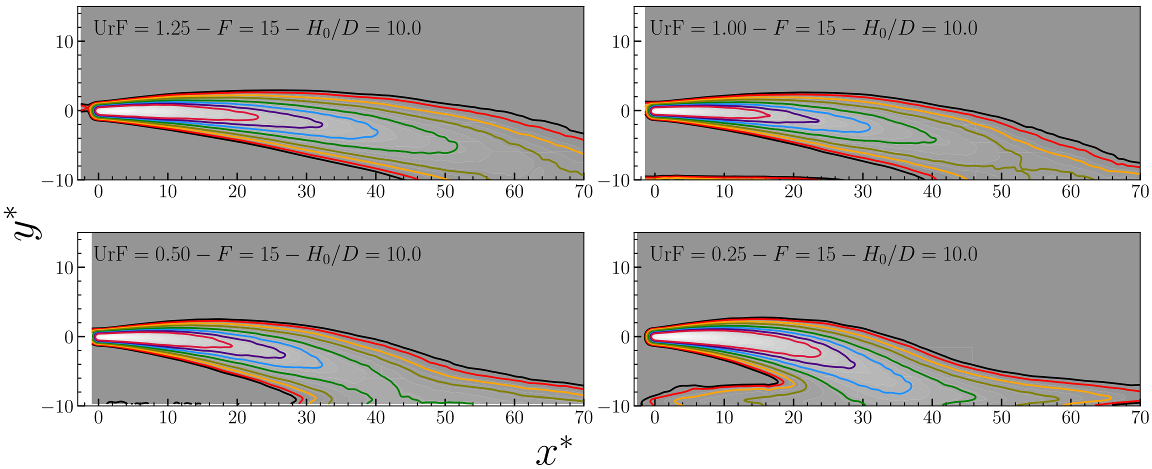

Fig. 3. Co-flow scenarios for $H_0/D = 10.0$ and $F = 15$. Counter lines represent iso-concentration values of 0.5, 0.4, 0.3, 0.2, 0.1, 0.05, 0.02, and 0.01.

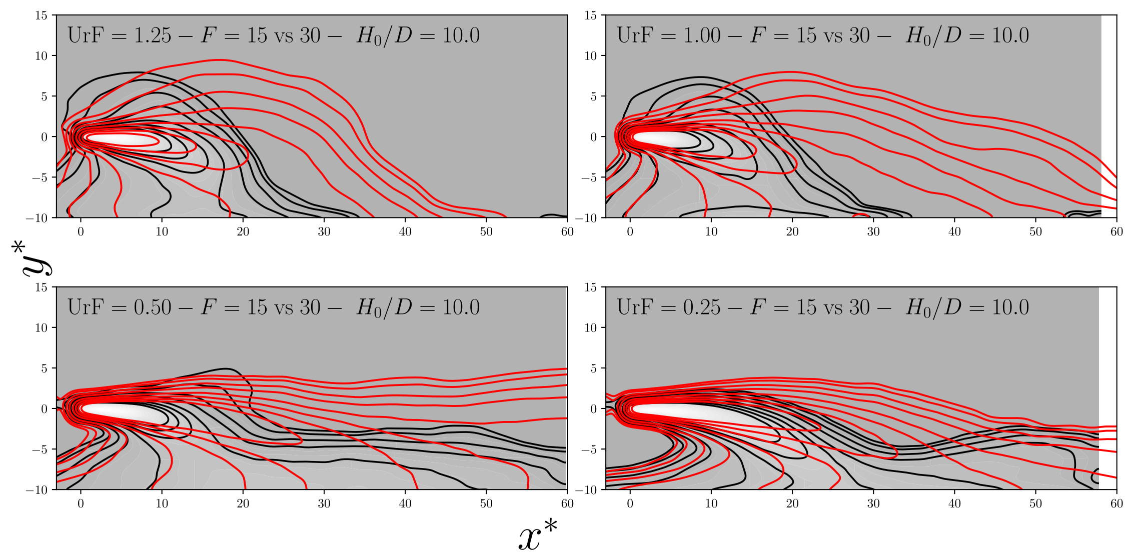

Fig. 4. Froude number effects on the flow patterns in cases with different U_rF values and $H_0/D = 10.0$ in counter-flow scenarios. —: F = 30 and —: F = 15. This figure contains supplementary materials.

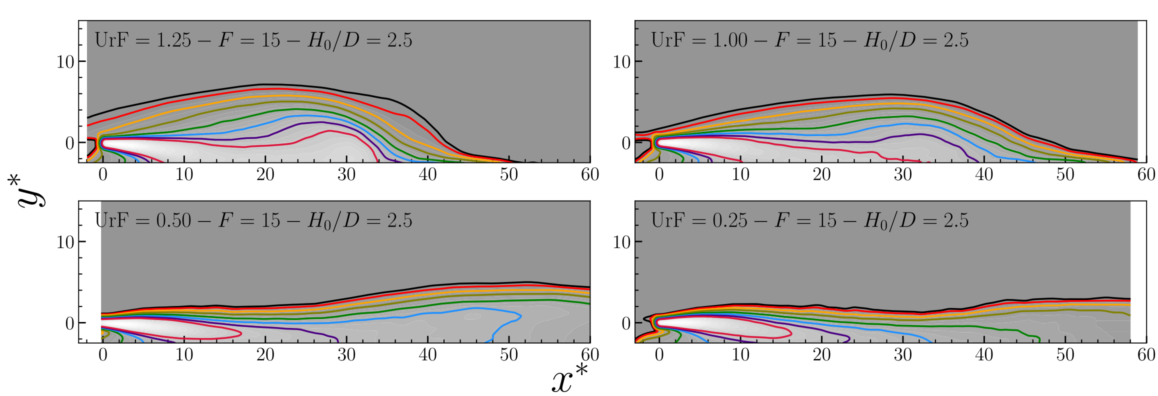

Fig. 5. Counter-flow scenarios for $H_0/D = 2.5$ and $F = 15$. Counter lines represent iso-concentration values of 0.5, 0.4, 0.3, 0.2, 0.1, 0.05, 0.02, and 0.01.

repeatability. These cases are therefore not considered representative of the underlying flow behavior and are omitted to preserve clarity and consistency in the presented results.

In the region where $x^* < F$ (Figs. 6, 8, and 10), after the concentration decays collapse based on the Froude-number regime, both co-flow and counter-flow cases become increasingly influenced by the current Froude number U_rF and the confinement ratio H_0/D. For the lowest confinement ratio, $H_0/D = 2.5$, the co-flow cases consistently exhibit a faster centerline decay across all U_rF values. As the confinement decreases, the influence of U_rF becomes more pronounced. For $H_0/D = 5.0$ and 10.0, the highest current Froude number $U_rF = 1.25$ leads to counter-flow cases decaying more rapidly than their co-flow

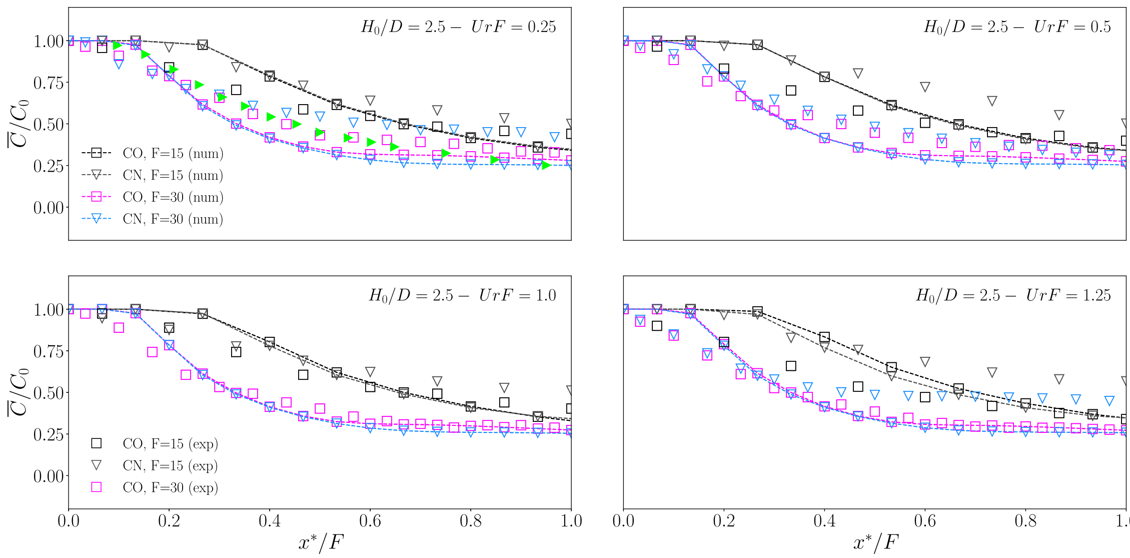

Fig. 6. Centerline concentration decay in all experimental and numerical scenarios for $H_0/D = 2.5$ and $x^* \leq F$. Legends are identical for all panels and are split for clarity. ▶ turbulent horizontal dense jet in stagnant ambient with $H_0/D = 3.0$ [66].

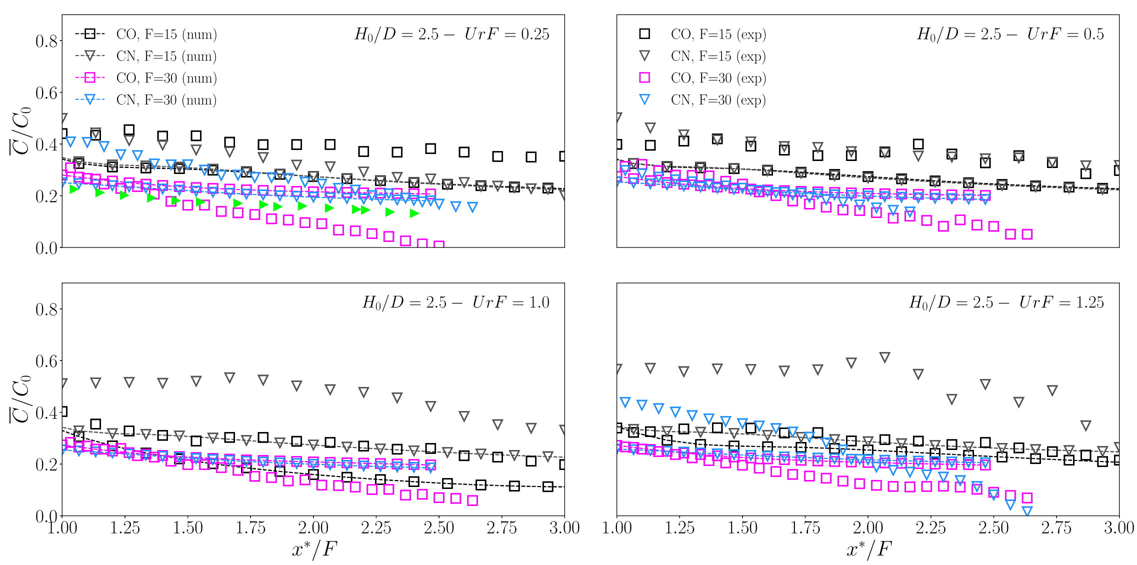

Fig. 7. Centerline concentration decay in all experimental and numerical scenarios for $H_0/D = 2.5$ and $x^* \geq F$. Legends are identical for all panels and are split for clarity. ▶ turbulent horizontal dense jet in stagnant ambient with $H_0/D = 3.0$ [66].

counterparts. In the least confined configuration, $H0/D = 10.0$ and for $F = 15$, the counter-flow scenarios generally show a faster decay than the corresponding co-flow cases in almost all U_rF values. For $F = 30$, this behavior is observed only when $U_rF \geq 1.0$.

In the downstream region where $x^* \geq F$ (Figs. 7, 9, 11), as x^* increases, the influence of the densimetric Froude number diminishes, while the role of the current Froude number U_rF becomes more evident. In the most confined configuration, $H_0/D = 2.5$, the counter-flow cases with $U_rF \geq 1.0$ exhibit the smallest decay rates. Under this regime (characterized by strong confinement and strong ambient-flow effects), the jet develops a recirculation zone and becomes unstable. This results in a less decayed centerline concentration, compared to the co-flow scenarios. This behavior is especially evident for the $F = 15$ scenarios at this confinement ratio.

As the confinement weakens (i.e. with increasing H_0/D), the relative influence of the counter-flow strengthens, and these cases transition to showing faster decay than their co-flow counterparts. While the co-flow cases maintain nearly uniform decay rates across U_rF, the counter-flow scenarios increasingly favor the less confined configurations, with higher U_rF producing noticeably faster decay. This behavior, which is accompanied by an out of plane oscillation, is examined in greater detail in Section 5.

Figs. 12 and 13 compare the co-flow and counter-flow conditions under different values of U_rF and confinement ratios H_0/D. The datasets in each panel are colored by their confinement ratio. The reference curves are from non-buoyant free [96] and wall jets [3]. In general, the co-flow cases exhibit a more asymptotic decay pattern, whereas the counter-flow cases show a sharper decline and stronger sensitivity to the confinement. For both flow conditions, the decay curves were divided into three regions, namely plateau, transitional, and tail, based on their behavior at each value of U_rF. Similar three-segment fittings were performed for the cases with $F = 30$. The resulting decay coefficients for all scenarios expressed using $\overline{C}/C_0 = a \cdot x^{*b}$ are shown in Figs. 12 and 13. These data are further summarized in Table 2.

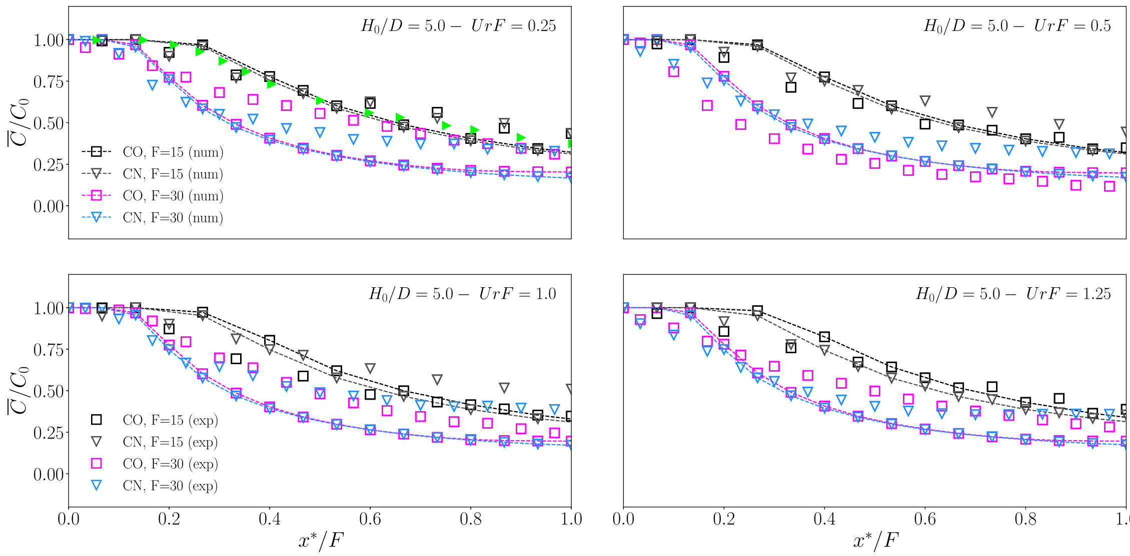

Fig. 8. Centerline concentration decay in all experimental and numerical scenarios for $H_0/D = 5.0$ and $x^* \le F$. Legends are identical for all panels and are split for clarity. ▶ turbulent horizontal dense jet in stagnant ambient with $H_0/D = 5.0$ [66].

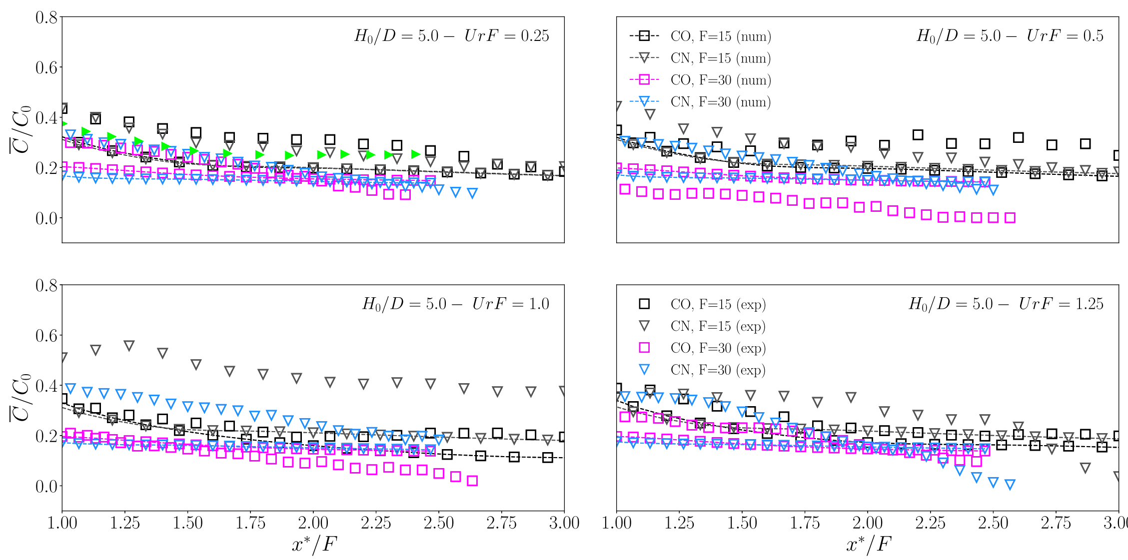

Fig. 9. Centerline concentration decay in all experimental and numerical scenarios for $H_0/D = 5.0$ and $x^* \ge F$. Legends are identical for all panels and are split for clarity. ▶ turbulent horizontal dense jet in stagnant ambient and $H_0/D = 5.0$ [66].

The extracted decay coefficients reveal three distinct behavioral classes. The plateau region is essentially universal across all configurations, with exponents restricted to b = 0.16-0.26. In contrast, the transitional zone exhibits clear regime dependence, forming three clusters: mild decay (b = 0.60-0.67) dominated by co-flow jets, moderate decay (b = 0.67-0.72) occurring across both flow types, and strong decay (b = 0.75-0.80) characteristic of counter-flow jets with large U_rF. In the far-field tail, the solutions collapse again into two families: a moderate-decay group (b = 0.50-0.63), mainly from F = 30 counter-flow and low-U_rF cases, and a strong-decay group (b = 0.68-0.80), comprising most F = 15 co-flow and high-U_rF counter-flow configurations.

Finally, Fig. 14 presents all experimental scenarios, colored by flow type and grouped across the three confinement ratios. This figure marks the global behavior of the jets under different co-flow and counter-flow conditions. For F = 15, the counter-flow cases increasingly dominate their co-flow counterparts as confinement intensifies. This effect is clearly visible when comparing the top-left and bottom-left panels. A similar trend appears for F = 30, although it becomes pronounced only at higher U_rF values. The figure also shows that for denser jets (i.e., F = 15), mixing improves under weaker confinement and larger current Froude numbers. In co-flow, the dilution develops in a more monotonic manner. Conversely, counter-flow becomes increasingly adverse to mixing in confined configurations (H_0/D = 2.5 and 5.0 here). From a practical perspective, these results indicate that ambient flow direction and confinement can significantly alter dilution performance in marine outfalls. Configurations that promote controlled interaction with ambient currents may enhance mixing, while excessive confinement or unfavorable alignment with the flow may reduce dilution efficiency.

4.3. Cross-sectional profiles

Figs. 15, 16, and 17 present the cross-sectional profiles of the normalized mass concentration at several downstream locations before and after impingement.

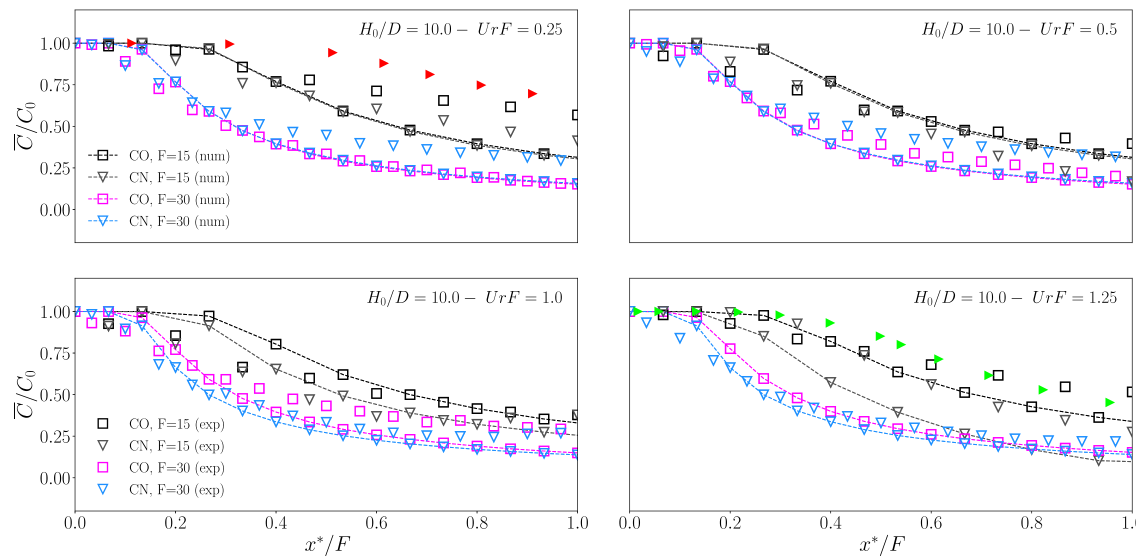

Fig. 10. Centerline concentration decay in all experimental and numerical scenarios for $H_0/D = 10.0$ and $x^* \leq F$. Legends are identical for all panels and are split for clarity. ▶ turbulent horizontal dense jet in stagnant ambient and $H_0/D = 5.0$ [66]. ▶ non-buoyant jet in counter-flow with $\alpha = 10.0$ [87].

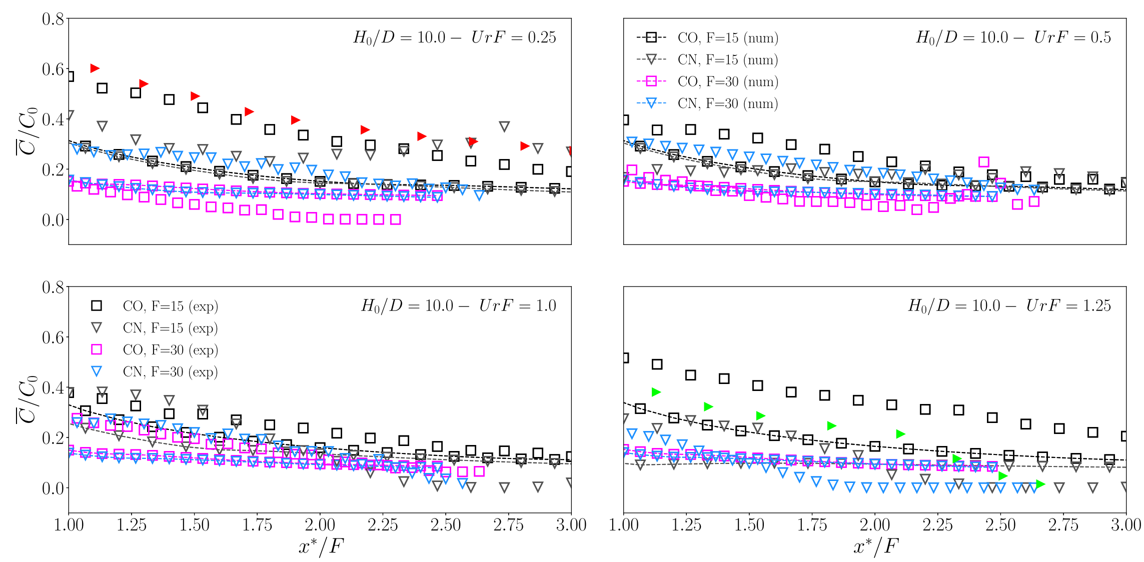

Fig. 11. Centerline concentration decay in all experimental and numerical scenarios for $H_0/D = 10.0$ and $x^* \geq F$. Legends are identical for all panels and are split for clarity. ▶ turbulent horizontal dense jet in stagnant ambient and $H_0/D = 5.0$ [66]. ▶ non-buoyant jet in counter-flow with $\alpha = 10.0$ [87].

Table 2
Unified classification of decay exponents (b) and corresponding x^*-ranges for the plateau, transitional, and tail segments.

Segment	Class	x^* range	b-range	Interpretation
Plateau	P	0–5	0.16–0.26	Universal weak decay; nearly flat profile, insensitive to F, U_rF, or flow type.
Transitional	T1	5–15	0.60–0.67	Mild decay; mostly CO and CN at $F = 30$, marking early-stage mixing growth.
	T2	5–15	0.67–0.72	Intermediate decay; mixed CO/CN regimes, associated with moderate U_rF.
	T3	5–15	0.75–0.80	Strong decay; CN dominated at $F = 15$,
Tail	C1	15–60	0.50–0.63	Moderate far-field decay; CN dominated, especially at $F = 30$.
	C2	15–60	0.68–0.80	Strong far-field decay; persistent current effects, typical of high U_rF.

For the case $H_0/D = 2.5$ and $U_rF = 1.25$, in Fig. 15, the strong confinement plays a dominant role in shaping the overall flow structure across all cross-sections. The proximity of the wall restricts vertical

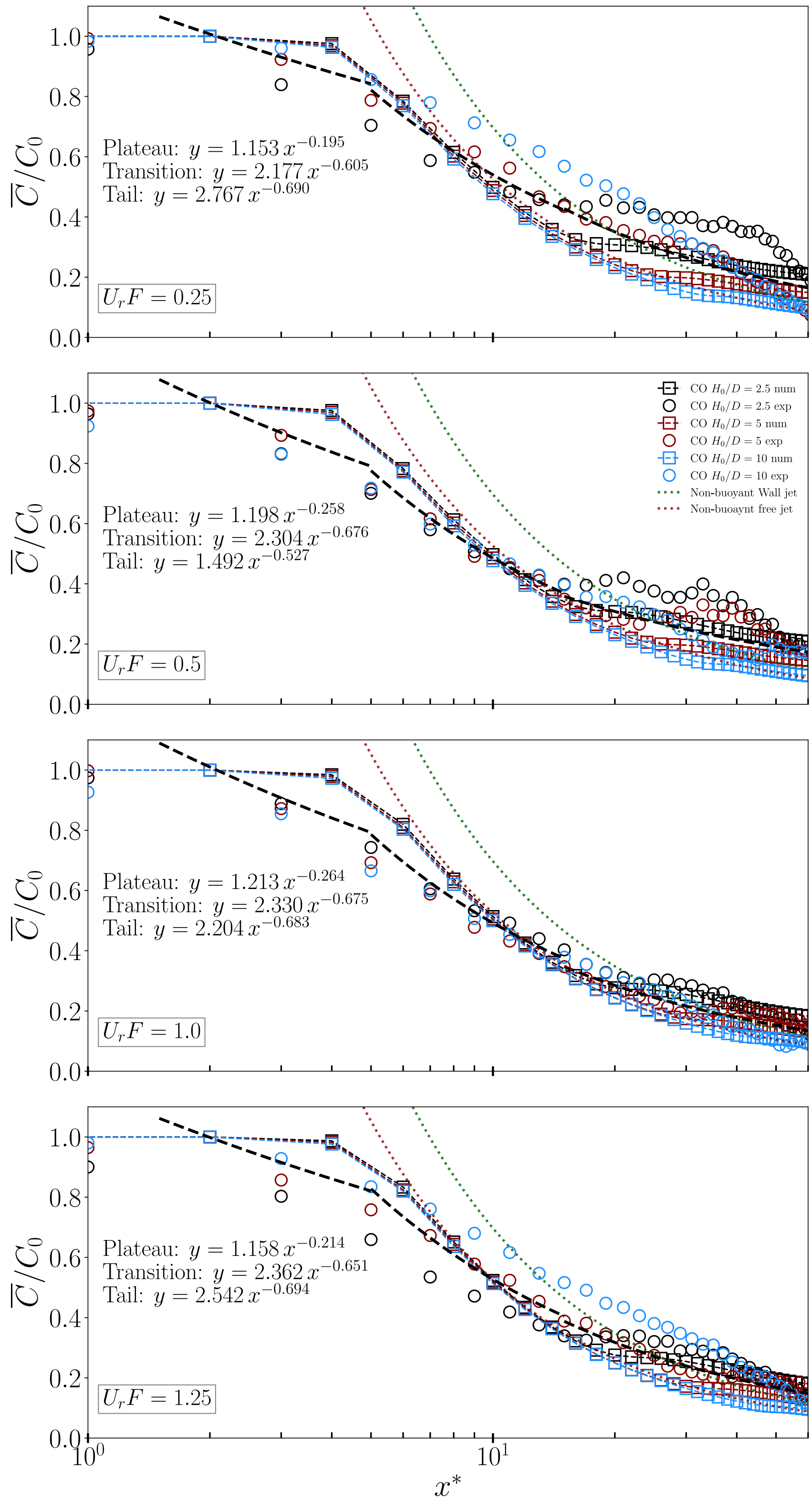

Fig. 12. Experimental and numerical scenarios under four different co-flow conditions and $F = 15$. Data is colorized based on H_0/D. [· · ·]: $6.97x^{-1}$ [3]; [· · ·]: $5.26x^{-1}$ [96].

development, thereby moderating the differences between co-flow and counter-flow configurations. Nevertheless, the influence of counter-flow is still evident. In the pre-impingement region, particularly at $x^* = 6$, the counter-flow profiles exhibit a wider distribution compared to the co-flow case, which remains close to the Gaussian shape. This indicates that the opposing ambient flow introduces asymmetry and enhanced spreading, although its development is limited by confinement. After impingement, the distinction between the two cases becomes more noticebale. The co-flow profiles tend to align with wall jet-like behavior, whereas the counter-flow profiles deviate from the wall jet similarity and appear more flattened. This behavior is attributed to

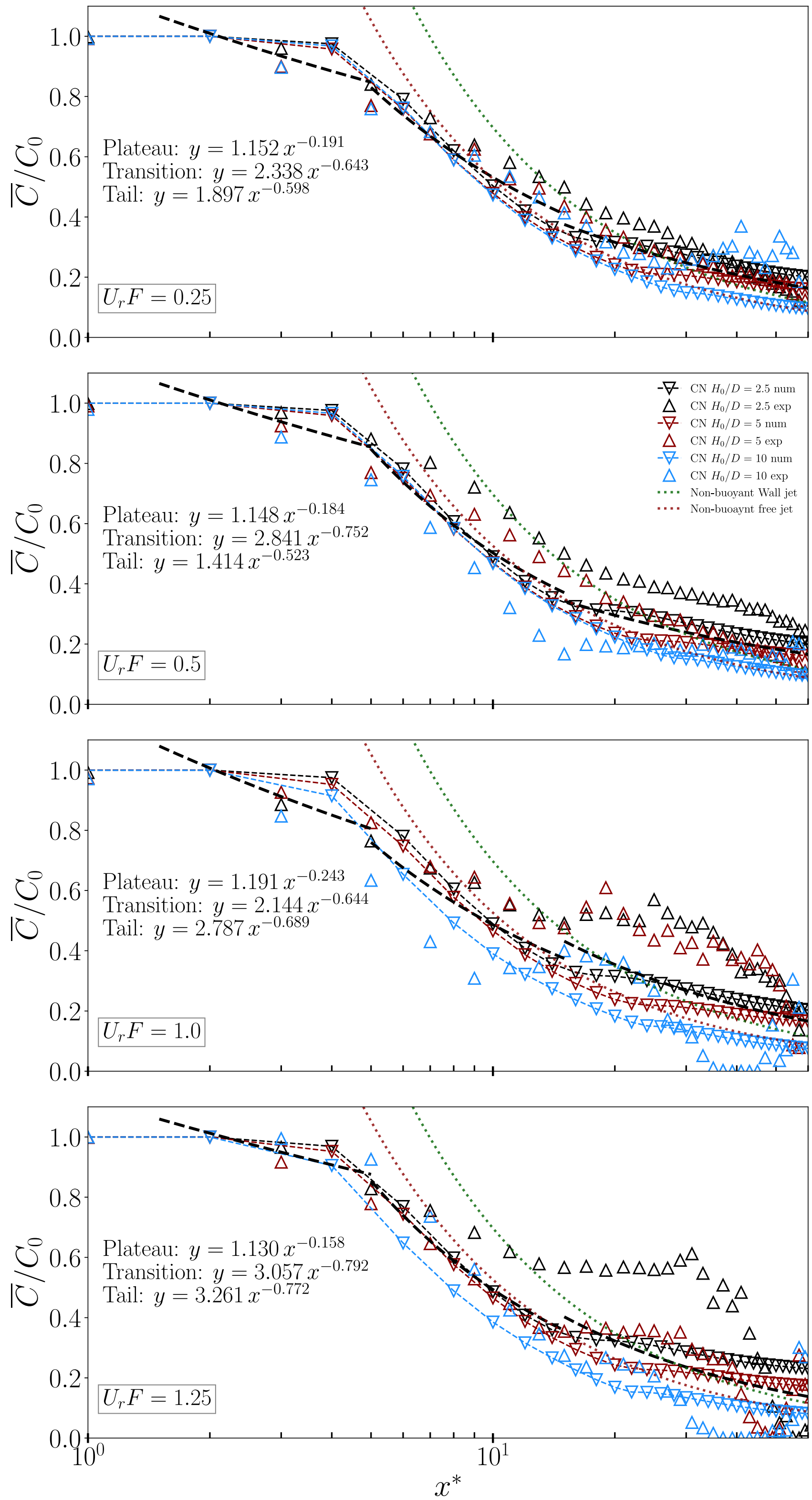

Fig. 13. Experimental and numerical scenarios under four different counter-flow conditions and $F = 15$. Data is colorized based on H_0/D. [· · ·]: $6.97x^{-1}$ [3]; [· · ·]: $5.26x^{-1}$ [96].

the combined effects of confinement and counter-flow, where the wall attached dense layer interacts with the opposing ambient flow above it, resulting in a broader vertical structure. In Fig. 16, with a larger offset $H_0/D = 5.0$ but the same $U_rF = 1.25$, the counter-flow profiles again fail to collapse onto wall jet similarity curves, suggesting that with increased confinement ratio, the counter-flow imprint is more significant. Meanwhile, the co-flow profiles continue to follow the Gaussian form across all measured sections. Finally, in Fig. 17, for the case with minimal confinement ($H_0/D = 10$) and weaker current velocity ($U_rF = 0.50$), the counter-flow influence is substantially diminished. Here, the profiles for both co- and counter-flow scenarios converge more

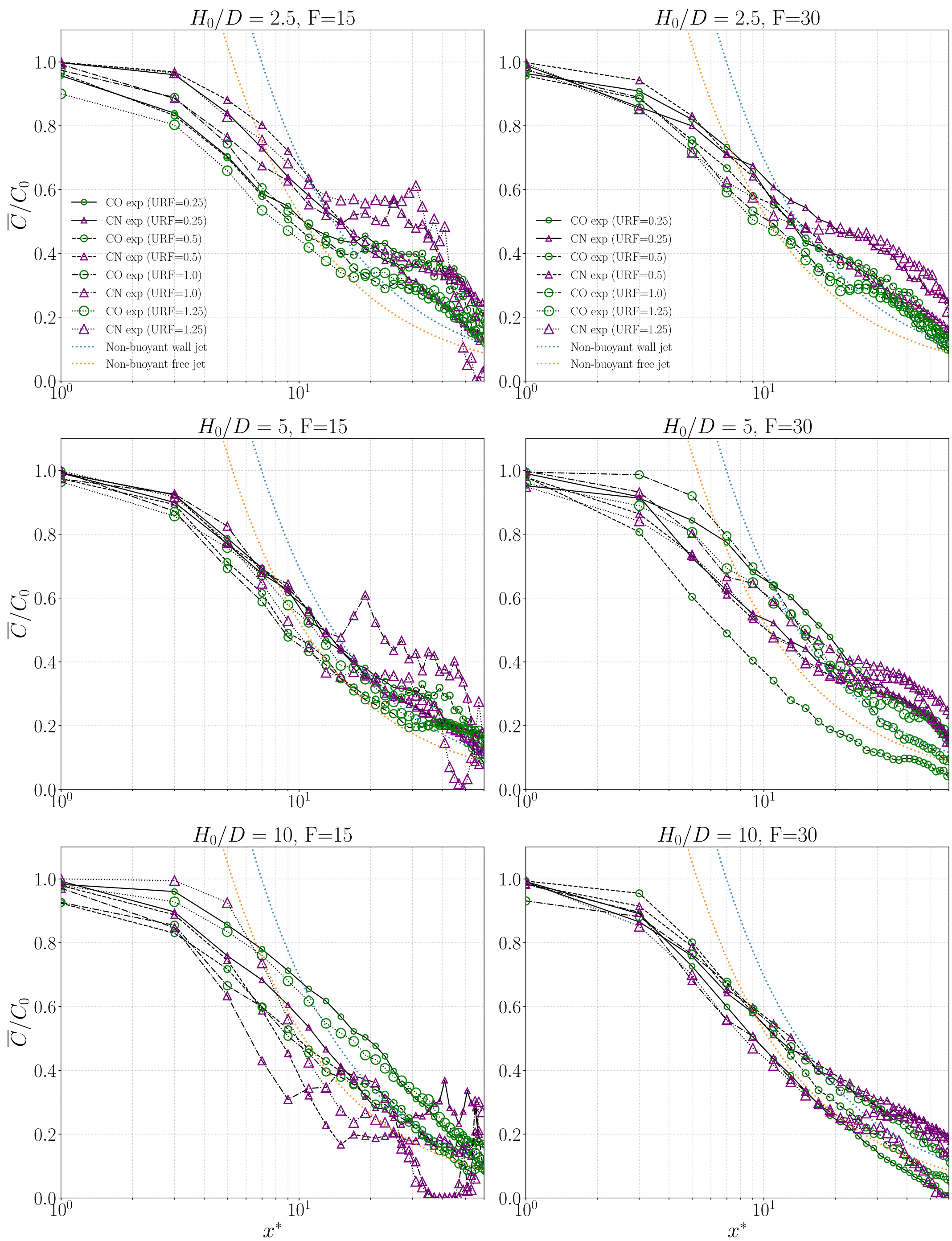

Fig. 14. Experimental co- and counter-flow scenarios in all configurations. ○ co-flow; △ counter-flow.

closely and demonstrate improved agreement with canonical similarity distributions, with the reduced influence of reverse flow direction. This behavior is governed by the combined effects of the confinement ratio H_0/D, the current Froude number U_rF, and the downstream evolution of the jet. The weak confinement ($H_0/D = 10$) allows the flow to expand with minimal wall interference, while the moderate ambient forcing ($U_rF = 0.50$) is insufficient to sustain strong counter-flow-induced asymmetry. Consequently, both flow configurations approach a density current structure.

5. Counter-flow instabilities

It is well established that jets issued into counter-flow conditions exhibit enhanced mixing compared to their co-flow counterparts [77,88,116]. This improvement is primarily attributed to the presence of low-frequency oscillations, which induce off-axis motion and contribute to greater lateral dispersion [77,80,81]. As a result, statistical mean flow variables and their fluctuations tend to spread more significantly across different realizations, spatial locations, and temporal averaging intervals.

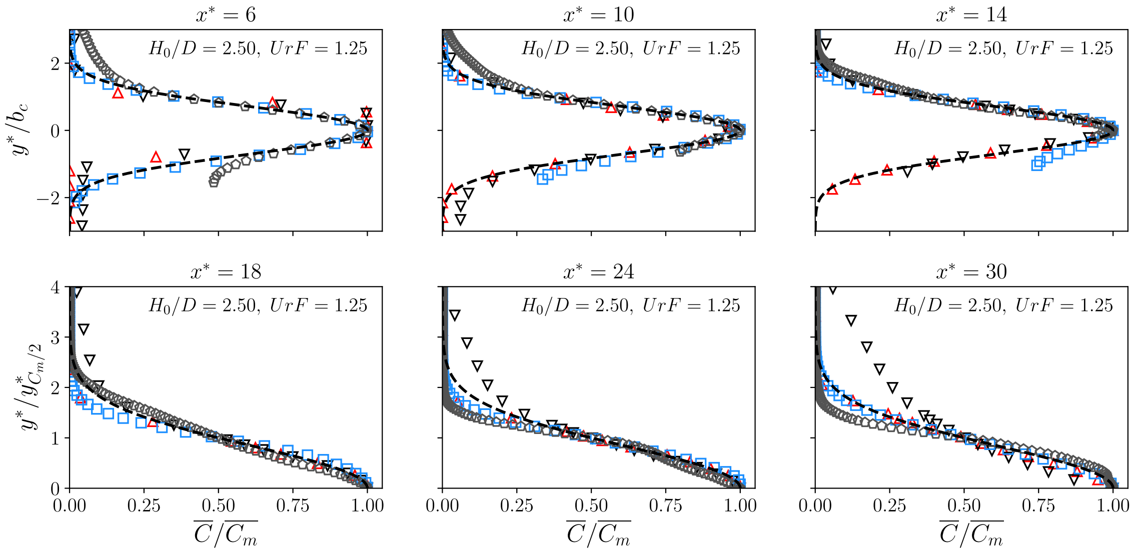

Fig. 15. Concentration cross-sectional profiles before and after impingement for cases with H_0/D = 2.5. □ CO (exp); ⬠ CN (exp); △ CO (num); ▽ CN (num); – – – Gaussian distribution.

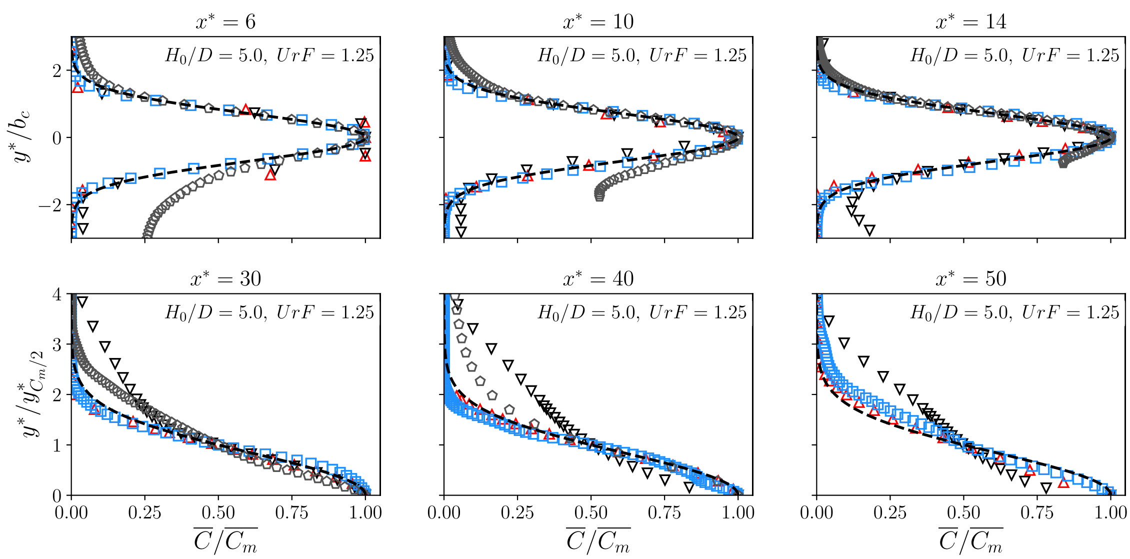

Fig. 16. Concentration cross-sectional profiles before and after impingement for cases with H_0/D = 5.0. □ CO (exp); ⬠ CN (exp); △ CO (num); ▽ CN (num); – – – Gaussian distribution.

Early insights into the flow dynamics of jets in counter-flow were provided by [88], who applied POD to experimental velocity data and identified two dominant modes of axial and radial oscillation at a velocity ratio of α = 3.4. Their findings were later supported by [117], who observed similar frequency peaks in the power spectra of the concentration field's centroid position. [82] applied POD to experimental data from jet discharged into counter flow at α = 4, 10, and 20, while in the present study are α = 12, 15, 20, and 30.

The following section focuses on dense jets discharged into counter-flow scenarios, with particular attention to the characteristic flapping behavior and its influence on mixing efficiency. Two representative current Froude numbers are examined: $U_r F = 0.25$, and 1.25.

Fig. 18 shows the least-confined configuration (H_0/D = 10), where the counter-flow jet exhibits a pronounced flapping motion characterized by large-scale vertical and lateral oscillations of the jet core. The instantaneous fields reveal alternating upward and downward deflections and a highly unsteady, irregular mixing envelope that forms and decays over time. This behavior reflects the susceptibility of an unconfined dense jet in counter-flow to global instabilities, which amplify when the ambient momentum opposes the jet but is not constrained by nearby boundaries.

In contrast, in the most-confined case (H_0/D = 2.5) as shown in Fig. 19, the bottom boundary suppresses the development of such global oscillations. The jet remains attached to the lower wall for most of its evolution, and the counter-flow interaction produces a more stable recirculation region that forms farther downstream. The mixing structure becomes vertically compact, and the large-scale flapping observed in the unconfined case does not develop. This demonstrates that confinement effectively damps the jet's natural instability modes, altering both the trajectory and the mixing pattern.

To quantify the flapping behavior observed in counter-flow scenarios, six representative cases were selected. These include the two extreme current Froude numbers, $U_r F$ = 0.25 and $U_r F$ = 1.25, combined with the smallest, medium, and largest confinement ratios, H_0/D = 2.5, 5, and 10 to evaluate the interplay between counter-flow strength and confinement on jet dynamics. The flapping behavior of the jet in counter-flow was quantified by evaluating the root mean square (RMS) of the centerline displacement amplitude at various streamwise

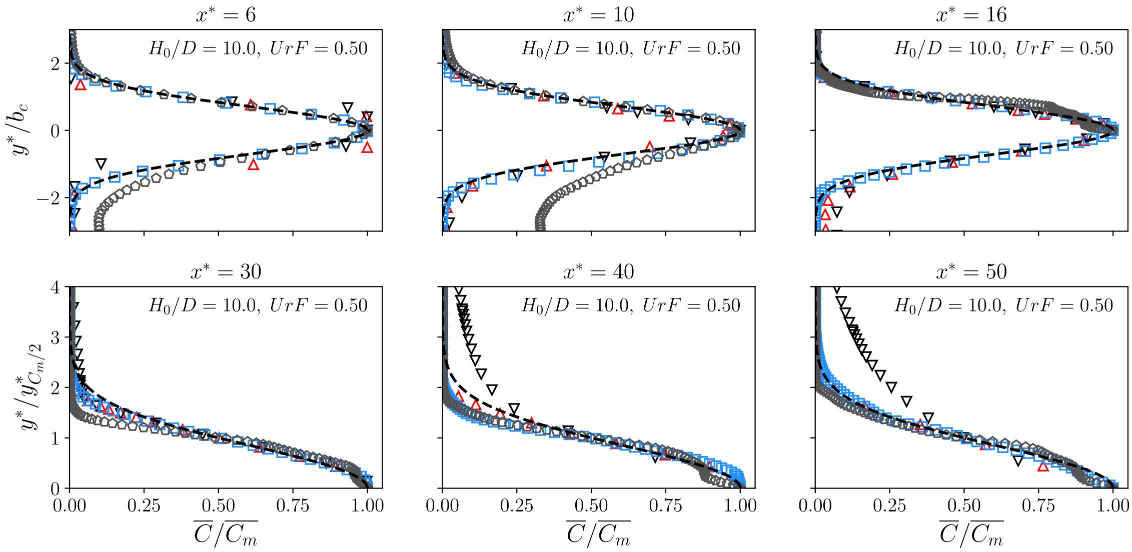

Fig. 17. Concentration cross-sectional profiles before and after impingement for cases with $H_0/D = 10.0$. □ CO (exp); ⬠ CN (exp); △ CO (num); ▽ CN (num); – – – Gaussian distribution.

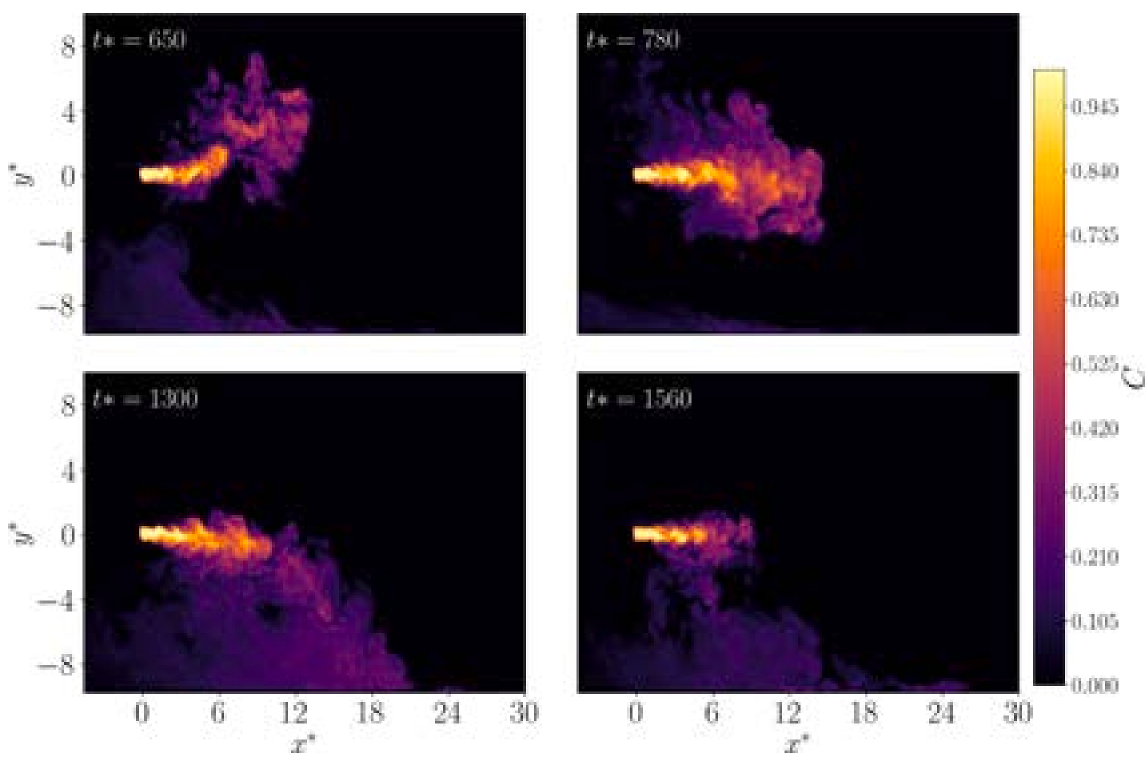

Fig. 18. General flow behavior in a counter-flow scenario with $F = 15$, $U_r F = 1.25$, and $H_0/D = 10$ illustrating characteristic flapping and mixing development. $t*$ in each panel represents the non-dimensional time progress. This figure contains supplementary materials.

locations x^*:

$$\overline{y'_c} = \sqrt{\frac{1}{N}\sum_{i=1}^{N}\left(y_c(t_i) - \overline{y_c}\right)^2}, \tag{23}$$

where $\overline{y_c}$ is the temporal mean of the centerline position,

$$\overline{y_c} = \frac{1}{N}\sum_{i=1}^{N} y_c(t_i). \tag{24}$$

This metric provides a direct measure of the extent of off-axis motion, with higher RMS values indicating stronger vertical deviations and increased unsteadiness. Fig. 20 presents the distribution of RMS amplitudes along the jet axis for the selected cases. As seen from the figure, the case with $H_0/D = 10$ and $U_r F = 1.25$, stands out, compared to the rest of the scenarios. Comes after that, is the case with $H_0/D = 5$ and the same current Froude number. It is interesting to note how the confinement can curb the flapping behavior as the case with the $H_0/D = 2.5$ and $U_r F = 1.25$, does not show a very distinct variation from their counterpart with the weakest current Froude number $U_r F = 0.25$.

The interaction between confinement and counter-flow dynamics was further investigated through spectral analysis of the centerline displacement time series. This analysis, are presented in detail in Appendix A.2. Notably, for counter-flow scenarios with low confinement

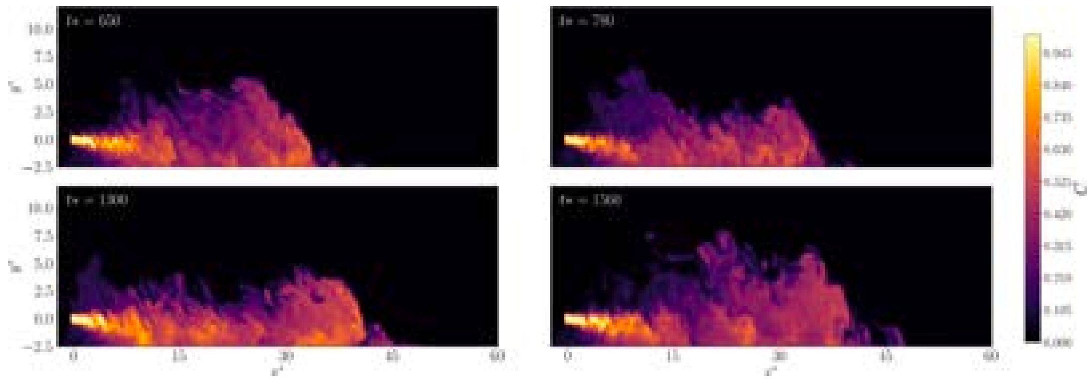

Fig. 19. General flow behavior in a counter-flow scenario with $F = 15$, $U_rF = 1.25$, and $H_0/D = 2.5$ illustrating characteristic flapping and mixing development. $t*$ in each panel represents the non-dimensional time progress.This figure contains supplementary materials.

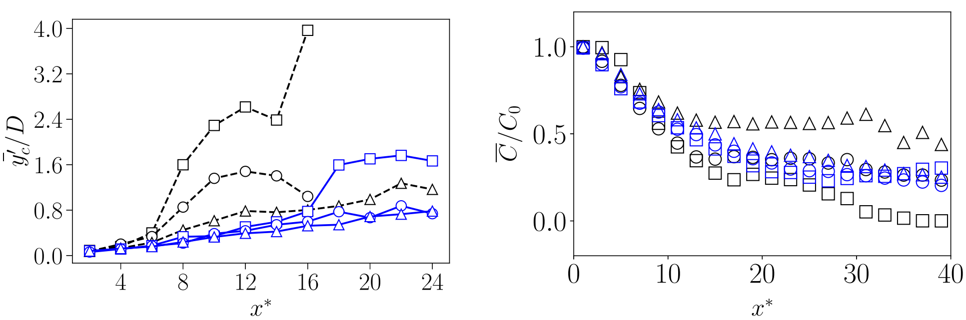

Fig. 20. RMS of the centerline displacement amplitude at various streamwise locations (left) along with the centerline decay for the selected counter-flow scenarios (right). □ $U_rF = 1.25 - H_0/D = 10.0$; ○ $U_rF = 1.25 - H_0/D = 5.0$; △ $U_rF = 1.25 - H_0/D = 2.5$; □ $U_rF = 0.25 - H_0/D = 10.0$; ○ $U_rF = 0.25 - H_0/D = 5.0$; △ $U_rF = 0.25 - H_0/D = 2.5$.

($H_0/D = 10$), a dominant low-frequency peak was observed in the power spectral density (PSD), indicating the presence of quasi-periodic flapping motion. This behavior aligns with the enhanced jet spreading and mixing observed in the time-averaged concentration fields.

In contrast, strongly confined counter-flow cases ($H_0/D = 2.5$) exhibited broader PSD distributions with energy spread over multiple low frequencies. This suggests intermittent flapping and mode switching, likely driven by intensified wall interactions. For co-flow scenarios, the spectral content shifted to higher frequencies, with patterns consistent with convective instabilities such as vortex shedding, particularly under weak confinement. For a complete discussion of the spectral analysis and corresponding plots on the counter-flow jet oscillation, see Appendix A.2.

These observations suggest that large-scale instabilities, such as flapping in counter-flow conditions, may play a beneficial role in enhancing mixing in environmental discharge systems. However, their sensitivity to confinement highlights the importance of diffuser placement in controlling both stability and dilution performance.

The counter-flow instability causes the jet to oscillate in a fully three-dimensional flapping motion [89,117]. In a two-dimensional measurement, however, only the in-plane evolution of the flow, including the lateral flapping and the oscillatory behavior, can be captured. Consequently, the jet development on the central plane does not represent the complete picture of mixing, especially as the current Froude number U_rF increases and three-dimensional motions intensify. To examine the redistribution of scalar mass occurring outside the measurement plane, the planar scalar mass integral is defined as

$$M(x^*) = \int_{y^*_{\min}}^{y^*_{\max}} C(x^*, y^*)\, dy^*. \tag{25}$$

Tracking M along the streamwise direction and its derivative dM/dx^* provides a convenient means to infer the net scalar gain or loss within the measurement plane. When $dM/dx^* > 0$, the plane accumulates scalar mass downstream. If $dM/dx^* \simeq 0$, the scalar content remains nearly constant. Conversely, $dM/dx^* < 0$ indicates a net loss of scalar from the plane, either through vertical entrainment or spanwise dispersion driven by three-dimensional motions.

Fig. 21 (left) presents dM/dx^* for the strongest and weakest counter-flow conditions, $U_rF = 1.25$ and 0.25, respectively, across the three confinement ratios $H_0/D = 2.5$, 5.0, and 10.0. As seen, the two cases with $U_rF = 1.25$ and $H_0/D = 2.5$ and 10.0 exhibit the largest oscillations of mass loss and gain compared with the other cases. For the most confined case $H_0/D = 2.5$, a pronounced decrease in dM/dx^* occurs within $x^* \simeq 22$–33 before gradually returning toward equilibrium near $x^* = 60$. This behavior suggests that the in- and out-of-plane mass exchange is shifted further downstream, consistent with the POD mode analysis (Fig. 27) that reveals a persistent spatial mode extending well beyond the nozzle region. The combined effects of wall proximity and opposing momentum appear to delay the onset of cross-plane motion until a downstream distance.

In contrast, the case with identical $U_rF = 1.25$ but weaker confinement, $H_0/D = 10$, displays a comparable pattern that occurs earlier along x^*, reflecting freer jet expansion and earlier onset of three-dimensional instability. Cases with $U_rF = 0.25$ exhibit much smaller variations in dM/dx^*, as the counter-flow forcing is insufficient to trigger pronounced oscillations. These weaker current cases also reach a quasi-steady condition with $dM/dx^* \simeq 0$ sooner than their high-U_rF counterparts. The case with $H_0/D = 10.0$ and $U_rF = 0.25$ still shows mild in–out-of-plane exchange but at a far lower intensity, illustrating the combined influence of counter-flow instability and confinement on three-dimensional mixing.

Classical integral measures such as the displacement and momentum thickness [118] characterize shear layer development by integrating normalized velocity profiles over the transverse direction. The

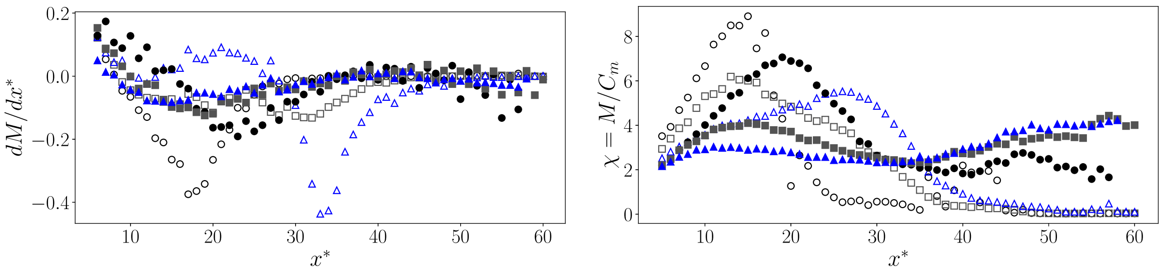

Fig. 21. Evolution of the scalar mass flux and integral scalar thickness in counter-flow cases. Left: streamwise derivative of the planar scalar mass, dM/dx^*. Right: Integral scalar thickness $\chi = M/C_m$. ∘ $U_rF = 1.25 - H_0/D = 10.0$; □ $U_rF = 1.25 - H_0/D = 5.0$; △ $U_rF = 1.25 - H_0/D = 2.5$;• $U_rF = 0.25 - H_0/D = 10.0$; ■ $U_rF = 0.25 - H_0/D = 5.0$; ▲ $U_rF = 0.25 - H_0/D = 2.5$.

displacement thickness,

$$\delta^* = \int_0^\infty \left(1 - \frac{U}{U_\infty}\right) dy, \tag{26}$$

represents the thickness of a uniform flow at velocity U_∞ that carries the same mass flow deficit as the actual boundary layer. The momentum thickness,

$$\theta = \int_0^\infty \frac{U}{U_\infty}\left(1 - \frac{U}{U_\infty}\right) dy, \tag{27}$$

is an inertia–weighted analogue that quantifies the effective thickness of the region responsible for momentum transport. In both cases, a non-uniform profile is replaced by an equivalent uniform slab whose width provides an integral measure of the layer's development.

Following this established framework, one can define the parameter

$$\chi(x^*) = \frac{M(x^*)}{C_m(x^*)} = \int \frac{C(x^*, y^*)}{C_m(x^*)}\, dy^*, \tag{28}$$

as an integral scalar thickness. The quantity χ represents the width of a uniform concentration layer of unit value that contains the same in-plane scalar mass as the true distribution. Unlike geometric measures such as the half-width or mean scalar profile thickness [119], χ incorporates the entire scalar profile and is therefore sensitive both to lateral spreading within the measurement plane and to out of plane scalar export associated with three-dimensional flapping in counter-flow scenarios.

Fig. 21(right) shows the evolution of $\chi(x^*)$ for counter-flow cases with strongest and weakest current Froude number U_rF. In a stagnant or weak co-flow configuration for a non-buoyant jet, χ would increase monotonically with downstream distance, analogous to the continuous growth of displacement thickness in canonical shear flows. In contrast, all counter-flow cases exhibit a non-monotonic behavior: χ initially increases as the scalar layer spreads within the measurement plane, and subsequently decreases once scalar mass is transported out of the plane by the onset of three-dimensional flapping. The location of this increase–decrease transition depends strongly on both the confinement ratio H_0/D and the current Froude number U_rF. The strongly confined case ($H_0/D = 2.5$, $U_rF = 1.25$) maintains an increasing χ up to $x^* \simeq 30$, indicating delayed destabilization due to wall suppression of counter-flow flapping. Once confinement effects weakens, χ drops sharply. This reveals rapid scalar export from the measurement plane. Under weaker confinement ($H_0/D = 10$ at the same U_rF), the rise and subsequent decline in χ occur much earlier which is consistent with earlier transition to three-dimensional instability. Cases with lower U_rF exhibit same variations in χ, but in a different pace.

6. POD analysis

Proper orthogonal decomposition (POD) is a modal-decomposition technique that extracts the most energetic coherent structures from an ensemble of instantaneous velocity or scalar fields. It is particularly effective for turbulent flows, as it identifies orthogonal (independent) spatial modes and their associated temporal coefficients which represent dominant dynamics in the system (e.g., [76,120]). In this study, the snapshot method, in which a series of instantaneous fields are collected was used. The mean field is subtracted, and the resulting fluctuating fields are assembled into a correlation (or covariance) matrix. The eigenvectors of that matrix yield spatial POD modes and their eigenvalues quantify the captured variance (energy) in each mode (e.g.,[121,122]).

The snapshot POD method, introduced by [121], is suited for analyzing large datasets with high spatial resolution and comparatively fewer time instances. In this formulation, the scalar concentration field $c(\boldsymbol{x}, t)$ is decomposed into a mean component and a fluctuating part:

$$c(\boldsymbol{x}, t) = \bar{c}(\boldsymbol{x}) + c'(\boldsymbol{x}, t) \tag{29}$$

where $\bar{c}(\boldsymbol{x})$ is the time-averaged scalar concentration field, and $c'(\boldsymbol{x}, t)$ is the fluctuation.

Let $c_i'(\boldsymbol{x})$ denote the ith snapshot of the fluctuation field, and assume N available snapshots. The snapshot method constructs an $N \times N$ correlation matrix:

$$\mathbf{C}_{ij} = \langle c_i'(\boldsymbol{x}), c_j'(\boldsymbol{x})\rangle = \int_\Omega c_i'(\boldsymbol{x}) c_j'(\boldsymbol{x})\, d\boldsymbol{x} \tag{30}$$

Solving the eigenvalue problem,

$$\mathbf{C}\boldsymbol{a}^{(k)} = \lambda_k \boldsymbol{a}^{(k)} \tag{31}$$

yields the eigenvalues λ_k (mode energy) and eigenvectors $\boldsymbol{a}^{(k)}$. The corresponding POD modes are then constructed as linear combinations of the original snapshots:

$$\phi^{(k)}(\boldsymbol{x}) = \frac{1}{\sqrt{\lambda_k}} \sum_{i=1}^{N} a_i^{(k)} c_i'(\boldsymbol{x}) \tag{32}$$

Each fluctuating field can thus be reconstructed as:

$$c'(\boldsymbol{x}, t) = \sum_{k=1}^{N} a^{(k)}(t) \phi^{(k)}(\boldsymbol{x}) \tag{33}$$

where $a^{(k)}(t)$ are the time coefficients projecting the snapshots onto the spatial modes. These coefficients can be further analyzed in the frequency domain (e.g., via FFT) to identify dominant behavior.

Figs. 22 and 23 present the first six POD modes for the counter-flow and co-flow cases with $U_rF = 1.25$ and $H_0/D = 10.0$, respectively. From Fig. 22, in the counter-flow scenario, the Mode 1 reveals a strong anti-symmetric structure pair, indicative of a flapping instability that deflects the jet centerline. The lower lobe appears more pronounced than the upper one, due to the downward deflection tendency of the dense jet. Mode 2 closely resembles Mode 1 but appears shifted, which together with Mode 1 captures the oscillatory dynamics of the jet flapping. Modes 3 and 6 are more spatially compact, suggesting smaller-scale vortical activity associated with shear layer instabilities. Mode 4 exhibits a broader structure with large-scale features on both sides of the jet. Finally, Mode 5 shows minimal spatial gradients, which can be attributed to background long time fluctuations unrelated to

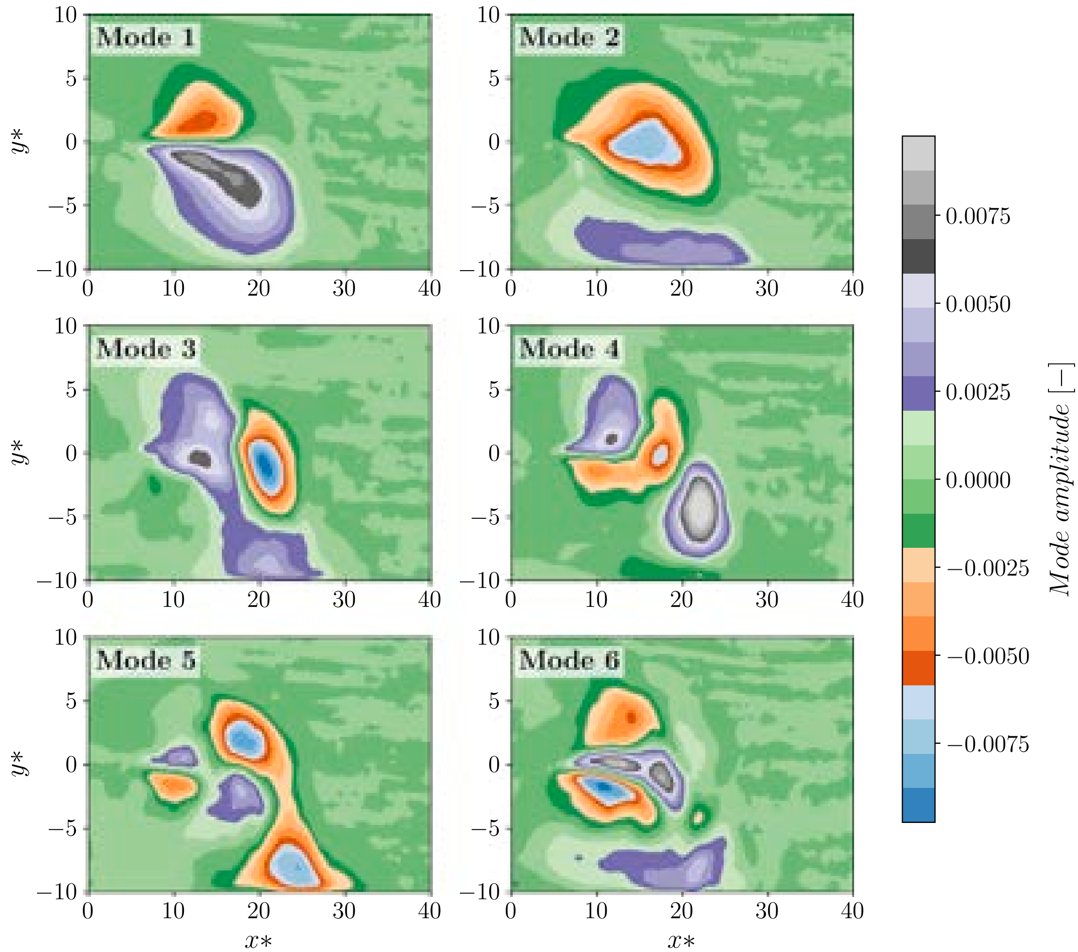

Fig. 22. First six spatial modes of a counter-flow scenario with $U_rF = 1.25$ and $H_0/D = 10.0$.

specific coherent structures. It should be noted that the interpretation is not based solely on the spatial structure of the POD modes. It is further supported by the spectral analysis presented in Appendix A.3

The spatial modes from the co-flow case, shown in Fig. 23, exhibit different characteristics. Mode 1 presents two broad, vertical lobes on either side of the jet, suggesting a slow vertical displacement of the entire jet column rather than a coherent periodic flapping. Mode 2 marks the onset of alternating structures above and below the jet, which resemble convective streaks that propagate downstream. These patterns are aligned with shear layer dynamics as suggested by [123] that POD modes in pair indicative of convected coherent structures. Modes 3 and 4 also display alternating signs and spatial distributions reminiscent of Mode 1, further reinforcing the presence of large-scale vertical deviations rather than sharp, periodic motion. Modes 5 and 6 exhibit finer-scale alternating spatial structures compared to the lower-order modes, with a larger number of lobes along the shear layer. Despite this visual similarity, the temporal characteristics of these modes differ markedly. As shown by the PSD analysis in Appendix A.3, Mode 5 is associated with a very low dominant frequency, indicating that it does not represent a convective shear layer instability but rather a slowly varying or quasi-stationary structure. In contrast, Mode 6 combines finer spatial scales with a higher dominant temporal frequency, making it a stronger candidate for capturing convective type instabilities within the shear layer.

To further evaluate the dynamical behavior of each POD temporal mode $a_k(t)$, spectral characteristics were extracted using power spectral density (PSD) analysis. Full methodological details and metric definitions are provided in Appendix A.3. In the counter-flow configuration, the first two modes exhibit dominant low-frequency content, capturing the large-scale flapping motion of the jet column with strong coherence and energy localization. These modes form a characteristic global oscillation. In contrast, the corresponding modes in the co-flow scenario display lower coherence and broader spectral content, suggesting a suppression of flapping and the redistribution of energy across less organized dynamics.

Higher-order modes further highlight differences between the two flow regimes. In the counter-flow, intermediate modes exhibit narrowband higher-frequency components linked to shear layer instabilities. Meanwhile, in the co-flow case, these modes become more dispersed, dominated by weaker, broadband features, or in some instances, shifted to even higher frequencies associated with small-scale periodic behavior.

These spectral distinctions reinforce that counter-flow encourages large-scale, low-frequency jet oscillations, while co-flow promotes spatially and temporally localized dynamics, driven by more stable shear layer development.

Because the snapshot correlation matrix C_{ij} is constructed from inner products of the fluctuating scalar fields (Eq. (30)), its eigenvalues quantify the variance (or fluctuation energy) associated with each orthogonal direction in snapshot space. Consequently, the POD modes are optimally ranked in decreasing energy, making them particularly suitable for reduced order representation [122].

Fig. 24 compares the cumulative modal energy for the counter- and co-flow cases. In the counter-flow configuration, the first two modes alone contribute approximately 45% of the total fluctuating energy, and the first 50 modes reach nearly 75%. This sharp concentration of energy in a few leading modes is consistent with the strong, coherent global oscillation imposed by the opposing ambient flow. In contrast,

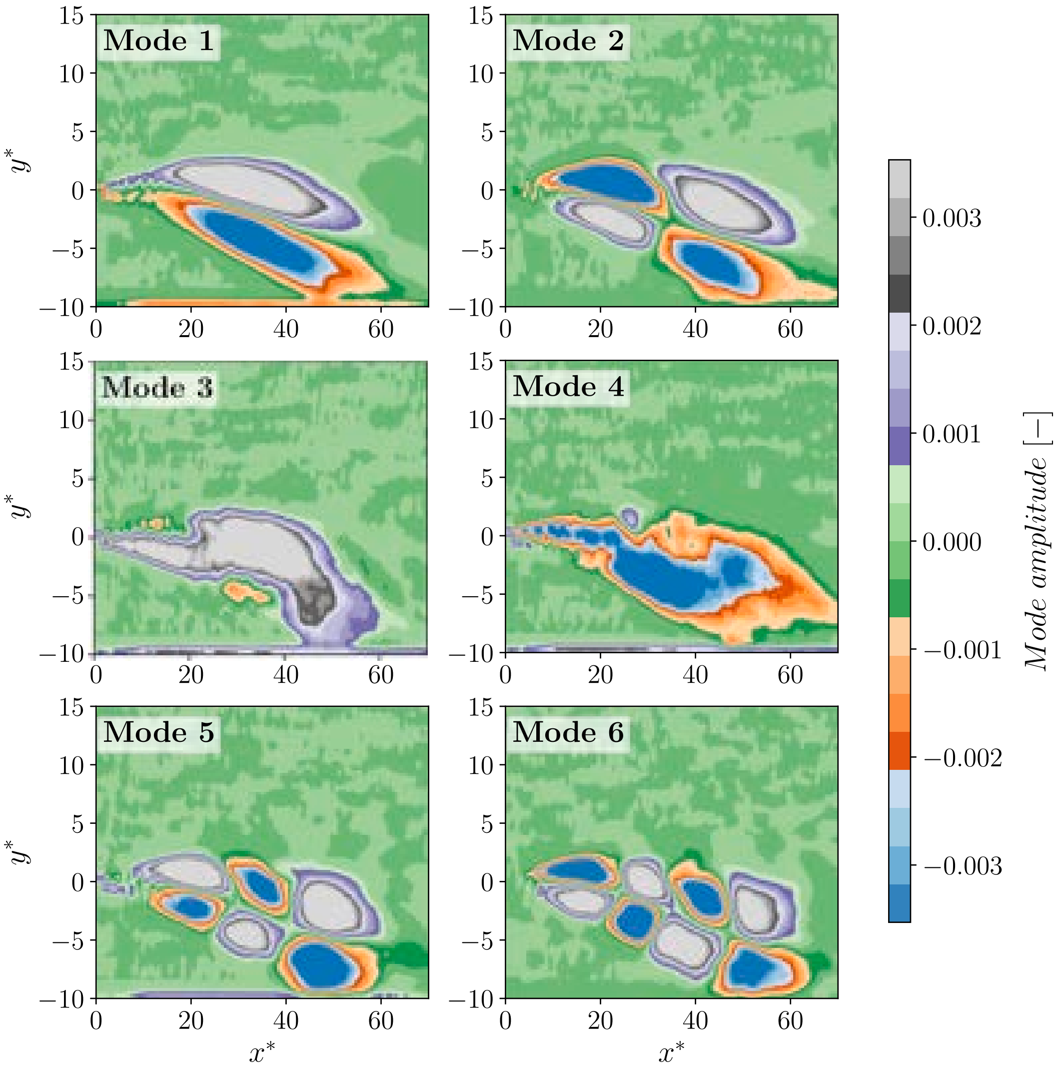

Fig. 23. First six spatial modes of a co-flow scenario with $U_rF = 1.25$ and $H_0/D = 10.0$.

the co-flow case exhibits a much more gradual accumulation of modal energy. The first 50 modes account for only about 35% of the total. The broader energy distribution reflects weaker global organization of the scalar field. Co-flow conditions disperse energy across a wider set of spatial structures.

The quantitative distribution of modal energy is summarized in Table 3. In the counter-flow case, a significant portion of the total energy is concentrated in the leading modes, with the first two modes capturing approximately 45% of the total energy and fewer than 50 modes accounting for nearly 80%. This indicates that the flow dynamics are dominated by a small number of coherent structures, consistent with the large-scale flapping motion observed in the instantaneous fields and POD modes. In contrast, the co-flow case exhibits a much more distributed energy spectrum, where the first two modes account for only about 6% of the total energy, and several hundred modes are required to capture the majority of the flow energy. This reflects a more gradual energy cascade across modes, indicating that the flow is governed by a broader range of smaller-scale structures rather than a few dominant coherent motions. These results demonstrate that the counter-flow configuration is characterized by energetically dominant large-scale instabilities, whereas the co-flow case exhibits a more diffuse and distributed turbulent structure. Consequently, the primary flow dynamics in counter-flow can be effectively represented using a limited number of modes, while a significantly larger number of modes is required to reconstruct the co-flow dynamics.

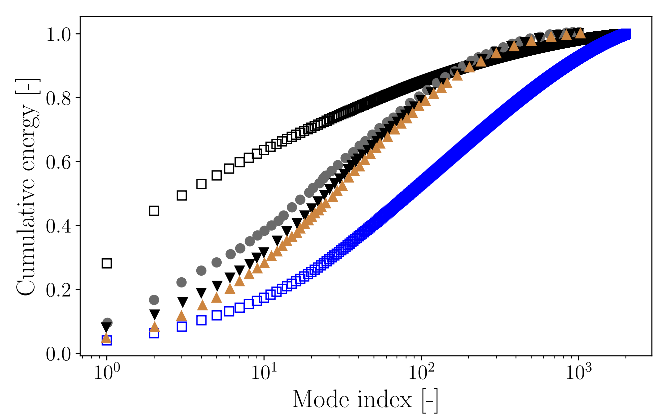

Fig. 24. Cumulative modal energy from counter-flow and co-flow scenarios compared with non-buoyant jets. □ CN, $U_rF = 1.25$, $\alpha = 12.0$, $H_0/D = 10.0$; □ CO, $U_rF = 1.25$, $\alpha = 12.0$. $H_0/D = 10.0$; Data from non-buoyant jet in counter flow [122]: • $\alpha = 4.0$; ▼, $\alpha = 10.0$; ▲ $\alpha = 20.0$.

POD-based reconstruction is a powerful means of assessing how efficiently dominant coherent structures represent the instantaneous dynamics of a flow. By rebuilding snapshots using a truncated set of modes, one can quantify the extent to which organized motions

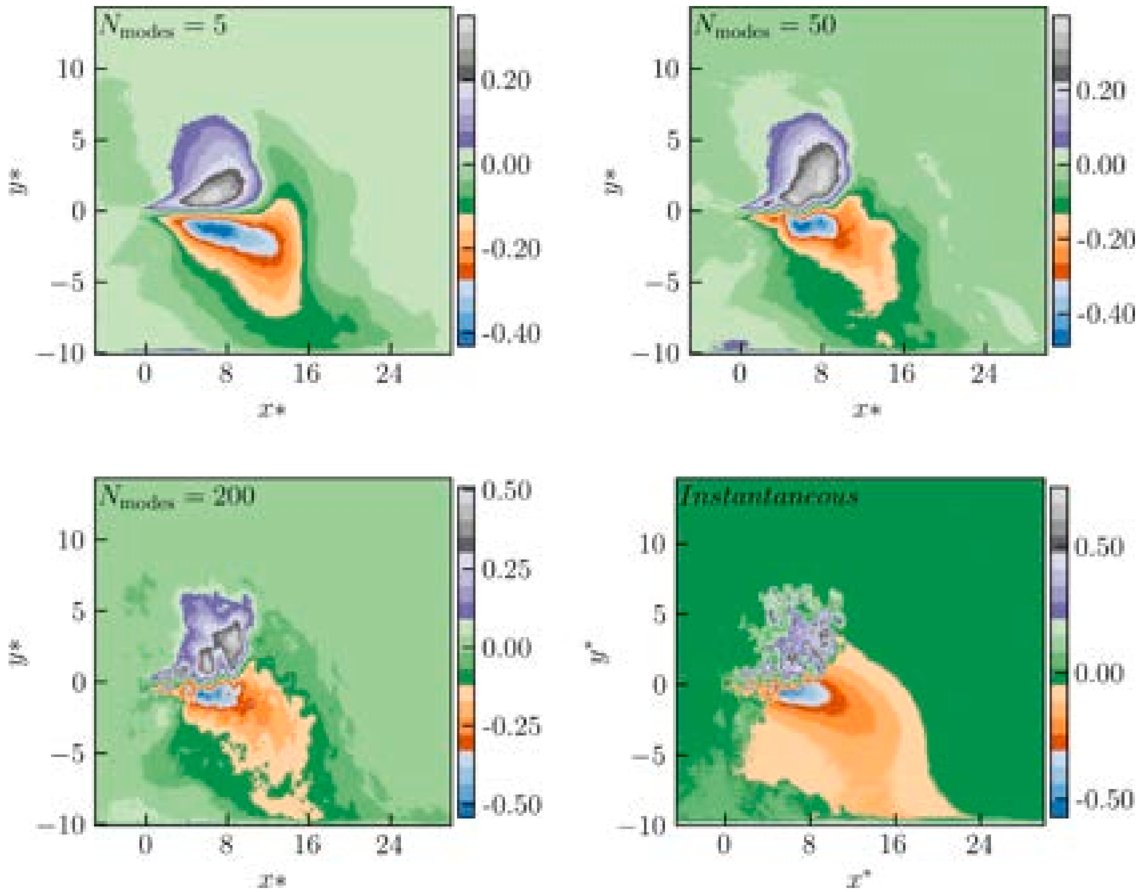

Fig. 25. Reconstructed concentration field using 5, 50, and 200 modes in comparison with the original instantaneous at the same realization. Counter-flow scenario: $U_r F = 1.25$, $H_0/D = 10.0$. Mean field is subtracted.

Table 3
Energy content of POD modes for the counter-flow (CN) and co-flow (CO) cases at $Fr = 15$, $U_r F = 1.25$, and $H_0/D = 10$.

Metric	CN	CO
Mode 1 energy [%]	28.14	4.02
Modes 1–2 energy [%]	44.61	6.27
Modes 1–5 energy [%]	55.67	11.86
Modes 1–10 energy [%]	63.63	17.39
Modes 1–50 energy [%]	79.18	40.50
Modes 1–100 energy [%]	85.02	53.17
Modes 1–200 energy [%]	89.95	66.01
Modes for 50% energy	4	85
Modes for 75% energy	32	329
Modes for 90% energy	202	831
Modes for 95% energy	483	1217

govern scalar transport. Here, reconstructed concentration fields were generated for both counter-flow and co-flow cases at $H_0/D = 10.0$, $U_r F = 1.25$, using 5, 50, and 200 number of modes (N_{modes}). The results are shown for counter-flow and co-flow in Figs. 25 and 26, respectively. In the counter-flow scenario (Fig. 25), the reconstruction with only five modes already reproduces the principal large-scale dipolar structure, including the characteristic upward high-concentration lobe and the complementary low-concentration feature beneath. This indicates that a small number of modes captures much of the scalar variance with the dominance of global flapping motion. Adding more modes progressively reveals intermediate scale entrainment and shear layer contributions, while 200 modes replicate the fine scale instantaneous field more accurately.

In the co-flow as shown in Fig. 26, the truncated reconstructions behave differently. With few modes, much of the jet structure is lost, and only weak localized features remain. Even at 50 modes, the structure remains fragmented, and only with 200 modes the reconstruction approaches the instantaneous field. These results demonstrate that counter-flow dynamics are governed by a strong global mode. Thus, low-order reconstructions to retain key features is applicable. Co-flow dynamics, however, lack a dominant large-scale signature, requiring many more modes to approximate the instantaneous state. This is in consistence with the previously discussed eigenvalues associated wih the POD modes as shown in Fig. 24.

To assess how proximity to the bed alters counter-flow behavior, POD-based reconstructions were performed for the case with identical current Froude number $U_r F = 1.25$ but smallest confinement ratio of $H_0/D = 2.5$. As seen from Fig. 27, similar to the low-confined configuration, the first few modes capture the dominant flapping motion. However, the resulting large-scale structure remains more strongly constrained to the near bed region, and the associated mixing is concentrated within a thinner jet envelope. Increasing the number of modes progressively restores small-scale shear layer structures but the near-wall confinement remains evident. These results indicate that reducing H_0/D suppresses the vertical flapping of the counter-flow jet and enhances wall affected organization.

7. Evaluation of numerical modeling and sources of errors

7.1. Evaluation of numerical modeling

A systematic comparison between the numerical predictions and their experimental counterparts was performed using the centerline

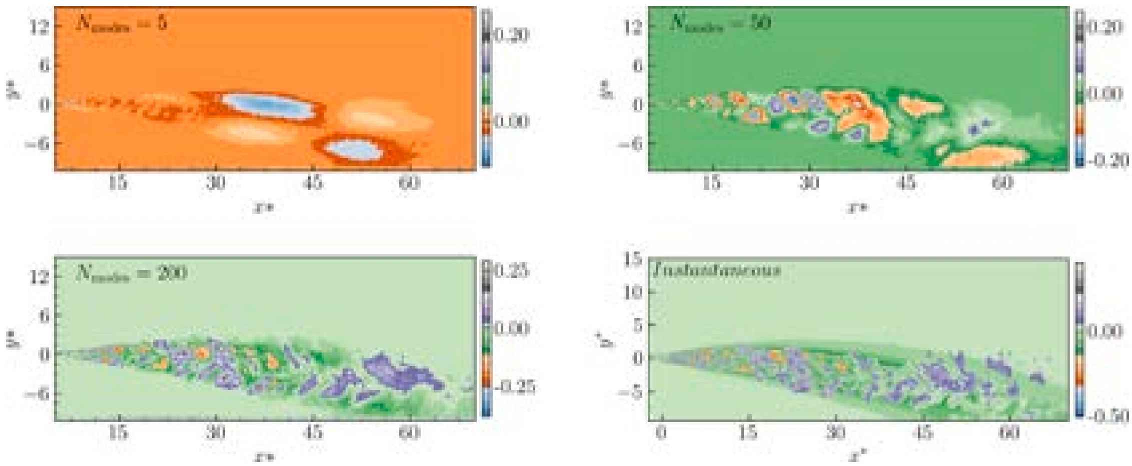

Fig. 26. Reconstructed concentration field using 5, 50, and 200 modes in comparison with the original instantaneous at the same realization. Co-flow scenario: $U_rF = 1.25$, $H_0/D = 10.0$. Mean field is subtracted. This figure contains supplementary materials.

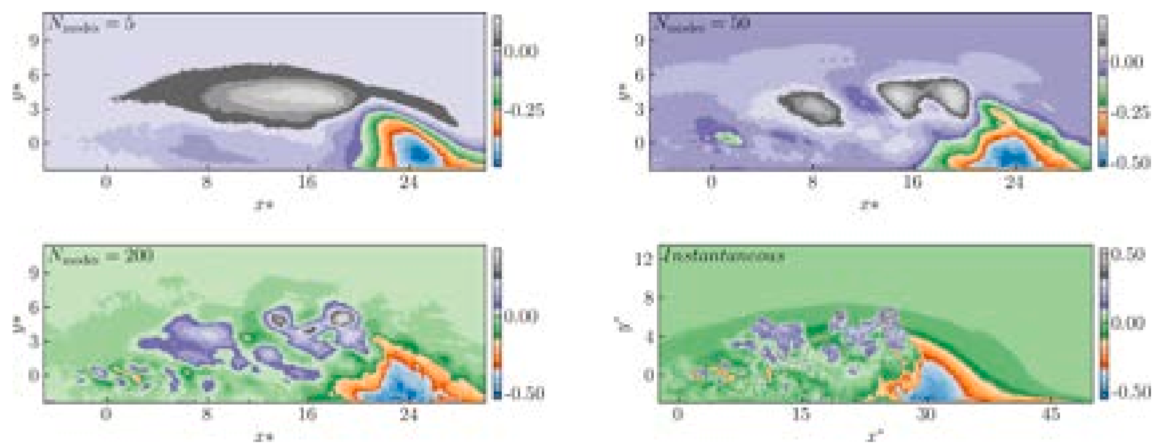

Fig. 27. Reconstructed concentration field using 5, 50, and 200 modes in comparison with the original instantaneous at the same realization. Counter-flow scenario: $U_rF = 1.25$, $H_0/D = 2.5$. Mean field is subtracted.

concentration decay across all confinement ratios, current Froude numbers, and both flow configurations (Figs. 6, 7, 8, 9, 10, and 11). The numerical model successfully reproduces the global trends of the decay process, including the relative ordering of co-flow and counter-flow cases, the influence of U_rF, and the transition between the plateau, transitional, and tail regions (as described in Table 2). In particular, in the upstream region ($x^* < F$), where the jet momentum dominates, the agreement between numerical and experimental results is generally good across all configurations.

Despite this agreement in trends, the simulations consistently exhibit a faster decay of centerline concentration compared to the experiments. This discrepancy becomes more evident in the downstream region ($x^* > F$), where ambient effects and flow instabilities play a more significant role. The overprediction of decay is especially evident in cases with higher current Froude numbers (U_rF) and weaker confinement, where counter-flow conditions induce strong unsteadiness and three-dimensional mixing. In these scenarios, the numerical model predicts a more rapid dilution than observed experimentally, suggesting an overestimation of turbulent mixing and scalar diffusivity.

The discrepancy is further amplified in the least confined configurations ($H_0/D = 10.0$), where the experimental data indicate a more gradual decay and partial persistence of concentration in the far field. In contrast, the numerical results exhibit a more monotonic and continuous decay, failing to capture the influence of large-scale coherent structures associated with counter-flow instabilities. Conversely, in strongly confined cases ($H_0/D = 2.5$), the experiments reveal reduced decay rates and, in some cases, plateau-like behavior due to the formation of recirculation zones and stabilization due to the wall proximity. The numerical model does not fully reproduce this behavior, instead continuing to predict progressive dilution downstream. A quantitative assessment of the centerline concentration decay was performed using the root-mean-square error (RMSE) and bias between numerical and experimental data, evaluated separately in the upstream ($x^*/F < 1$) and downstream ($x^*/F \geq 1$) regions (Table 4). The RMSE is defined as

$$\mathrm{RMSE} = \sqrt{\frac{1}{N}\sum_{i=1}^{N}\left(C_{\mathrm{exp},i} - C_{\mathrm{num},i}\right)^2}, \tag{34}$$

and the bias is defined as

$$\mathrm{Bias} = \frac{1}{N}\sum_{i=1}^{N}\left(C_{\mathrm{exp},i} - C_{\mathrm{num},i}\right), \tag{35}$$

where C_{exp} and C_{num} denote the experimental and numerical centerline concentrations, respectively, and N is the number of points used in the comparison. A positive bias indicates that the numerical model underpredicts the concentration (i.e. over-predicts dilution), whereas a negative bias indicates that the model over-predicts the concentration.

In the upstream region, the numerical results show moderate agreement with the experimental data, with RMSE values typically in the range of 0.05–0.15 and no consistent bias trend. In contrast, the downstream region exhibits systematically larger discrepancies, particularly in counter-flow cases and at higher U_rF, as explained before. The RMSE

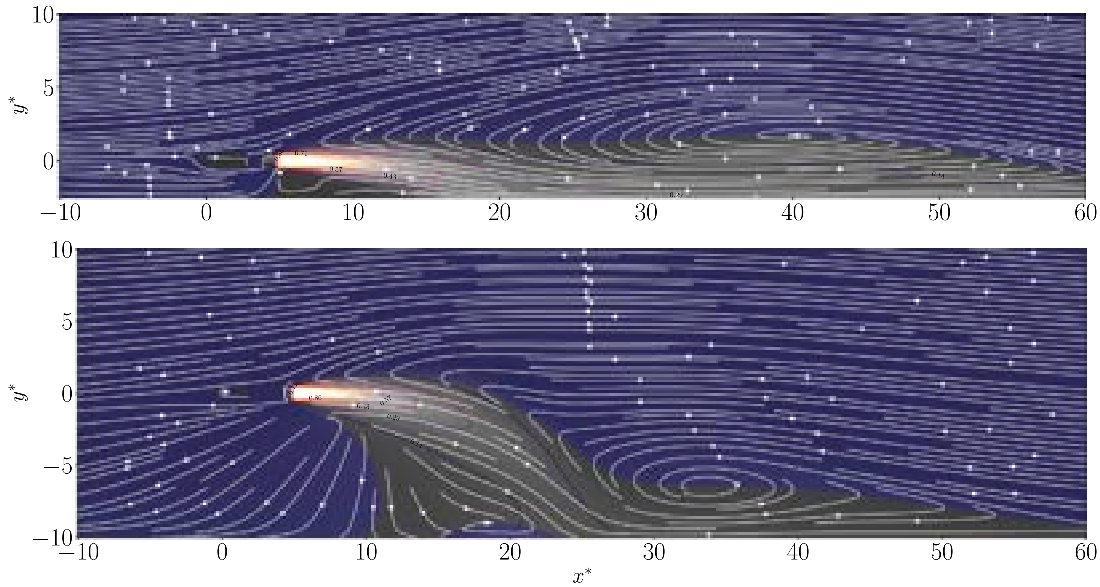

Fig. 28. Streamlines on the central x–y plane of the numerical cases with $U_rF = 1.25$, $F = 15$ in $H_0/D = 2.5$ (top), and $H_0/D = 10.0$, bottom. Both scenarios in counter-flow condition.

increases up to ≈ 0.20, and the bias is predominantly positive, indicating a consistent overprediction of concentration decay by the numerical model. This behavior is more pronounced for weaker confinement ($H_0/D = 10$), where large-scale flapping and instability-driven mixing dominate the flow dynamics.

Lastly, the use of the standard gradient diffusion hypothesis (SGDH) for scalar transport in the RANS framework inherently links the predicted mixing to the choice of the turbulent Schmidt number Sc_t. In the present study, a value of $Sc_t = 0.7$ was adopted, consistent with commonly recommended values for turbulent round jets [124]. Increasing Sc_t would reduce the modeled turbulent diffusivity and therefore decrease the overprediction of the concentration. However, numerical experiments performed during this study indicated that larger Sc_t values, while capable of lowering the dilution, adversely affect the accuracy of the jet trajectory and its geometrical evolution.

Fig. 28 shows the streamline fields extracted from the numerical model for two cases with $U_rF = 1.25$ and different confinement ratios ($H_0/D = 10, 2.5$). The results confirm that the RANS solver can qualitatively capture the global counter-flow behaviors in terms of the location of the primary recirculation zone, and the interaction between the jet and the opposing current.

A one-to-one comparison between all numerical and experimental cases for $F = 15$ is presented in supplementary materials.

7.2. Sources of errors

Several factors contribute to the uncertainties and errors in the experimental measurements. It should be noted that The experimental dataset does not include direct velocity measurements. As a result, any mismatch in the predicted entrainment or jet–current interaction is reflected in the scalar field.

The jet flow rate was controlled using an Omega rotameter (model FL46300), with a manufacturer-specified accuracy of ±5%. Since the instrument was operated with a saline solution denser than the calibration fluid, it was independently calibrated against a reference flowmeter (Transonic 400-series with TS410 tubing module), with additional verification through volumetric measurements. A calibration curve was established to relate the measured and actual flow rates. Furthermore, a single jet flow rate was maintained throughout all experiments, and the control valve was not adjusted once the desired flow condition was reached, ensuring consistent inlet conditions. The ambient velocity U_a was determined from the discharge measured using a rectangular weir, which depends on the estimation of the discharge coefficient C_d, the weir width L, and the head over the weir H. The uncertainty in U_a was estimated to be between 1.0% and 4%, based on comparison with velocity profiles measured using particle image velocimetry (PIV) in the same facility by [125]. Overall, the uncertainty in the experimental conditions is primarily associated with the estimation of the ambient velocity and, to a lesser extent, the jet flow rate.

8. Conclusion

This study presented an experimental and numerical investigation of offset dense jets under co-flow and counter-flow conditions across a range of confinement ratios. The key findings are summarized as follows:

- Ambient flow direction fundamentally alters the mixing behavior. Co-flow promotes smooth and monotonic dilution with relatively stable centerline trajectories, whereas counter-flow induces strong unsteadiness and low-frequency oscillatory behavior, particularly under weak confinement.
- Confinement modulates the development of instabilities and mixing. At strong confinement ($H_0/D = 2.5$), the counter-flow jet forms a recirculation zone that suppresses flapping, delays lateral spreading, and reduces downstream dilution. In contrast, weak confinement ($H_0/D = 10$) allows the development of large-scale oscillations that enhance entrainment and accelerate centerline decay.
- The POD analysis reveals a fundamental difference in flow organization between counter-flow and co-flow conditions. In counter-flow, a significant portion of the flow energy is concentrated in the leading modes, indicating that the dynamics are governed by a small number of large-scale coherent structures associated with flapping motion. In contrast, the co-flow cases exhibit a more distributed energy spectrum, with energy spread across higher-order modes, reflecting weaker coherence and a more gradual mixing process.
- Instability-driven oscillations in counter-flow enhance entrainment and three-dimensional scalar transport, leading to faster dilution under weak confinement. Conversely, strong confinement suppresses these mechanisms and delays mixing, resulting in reduced dilution efficiency.

Table 4
Quantitative error metrics for the centerline concentration decay. RMSE and bias are reported for upstream ($x^*/F < 1$) and downstream ($x^*/F \geq 1$) regions.

H_0/D	$U_r F$	Flow	F	RMSE (up)	Bias (up)	RMSE (down)	Bias (down)
2.5	0.25	CN	15.0	0.079	0.042	0.056	0.016
2.5	0.25	CN	30.0	0.167	0.121	0.088	0.075
2.5	0.25	CO	15.0	0.102	−0.056	0.098	0.063
2.5	0.25	CO	30.0	0.077	0.048	0.109	−0.09
2.5	0.5	CN	15.0	0.124	0.089	0.088	0.076
2.5	0.5	CN	30.0	0.103	0.074	0.03	−0.004
2.5	0.5	CO	15.0	0.104	−0.072	0.073	0.036
2.5	0.5	CO	30.0	0.083	0.034	0.066	−0.032
2.5	1.0	CN	15.0	0.097	0.01	0.165	0.144
2.5	1.0	CO	15.0	0.082	−0.044	0.083	0.071
2.5	1.0	CO	30.0	0.059	−0.011	0.066	−0.05
2.5	1.25	CN	15.0	0.116	0.074	0.213	0.058
2.5	1.25	CN	30.0	0.152	0.084	0.107	0.059
2.5	1.25	CO	15.0	0.156	−0.136	0.047	0.003
2.5	1.25	CO	30.0	0.069	−0.028	0.062	−0.053
5.0	0.25	CN	15.0	0.084	0.022	0.062	0.048
5.0	0.25	CN	30.0	0.115	0.068	0.088	0.067
5.0	0.25	CO	15.0	0.074	0.018	0.083	0.033
5.0	0.25	CO	30.0	0.167	0.132	0.063	0.034
5.0	0.5	CN	15.0	0.09	0.035	0.061	0.031
5.0	0.5	CN	30.0	0.1	0.044	0.079	0.057
5.0	0.5	CO	15.0	0.079	−0.05	0.076	0.062
5.0	0.5	CO	30.0	0.124	−0.104	0.104	−0.101
5.0	1.0	CN	15.0	0.099	0.042	0.203	0.178
5.0	1.0	CN	30.0	0.154	0.122	0.14	0.128
5.0	1.0	CO	15.0	0.103	−0.077	0.058	0.052
5.0	1.0	CO	30.0	0.122	0.107	0.046	−0.036
5.0	1.25	CN	15.0	0.036	−0.016	0.104	0.015
5.0	1.25	CN	30.0	0.111	0.049	0.114	0.064
5.0	1.25	CO	15.0	0.084	−0.039	0.051	0.046
5.0	1.25	CO	30.0	0.127	0.083	0.054	0.034
10.0	0.25	CN	15.0	0.083	0.014	0.148	0.138
10.0	0.25	CN	30.0	0.11	0.063	0.107	0.101
10.0	0.25	CO	15.0	0.148	0.1	0.131	0.082
10.0	0.25	CO	30.0	0.051	−0.016	0.074	−0.069
10.0	0.5	CN	15.0	0.094	−0.088	0.052	0.033
10.0	0.5	CN	30.0	0.122	0.082	0.116	0.11
10.0	0.5	CO	15.0	0.095	−0.053	0.077	0.07
10.0	0.5	CO	30.0	0.06	0.04	0.044	−0.011
10.0	1.0	CN	15.0	0.101	−0.073	0.104	0.021
10.0	1.0	CN	30.0	0.068	0.033	0.093	0.075
10.0	1.0	CO	15.0	0.112	−0.084	0.042	0.024
10.0	1.0	CO	30.0	0.109	0.063	0.069	0.052
10.0	1.25	CN	15.0	0.191	0.17	0.108	0.017
10.0	1.25	CN	30.0	0.063	0.02	0.072	−0.038
10.0	1.25	CO	15.0	0.096	0.042	0.121	0.1

- The numerical simulations reproduced the overall flow structure, including trajectory, curvature, and interaction with the ambient current, as confirmed by streamline comparisons. However, the model systematically over-predicts dilution, particularly at higher $U_r F$, due to limitations in scalar transport modeling.
- The observed differences between numerical and experimental results are primarily attributed to the sensitivity of scalar transport to the turbulent Schmidt number in the SGDH model, the absence of experimental velocity data for calibration, and uncertainties in the experimental conditions.
- From an engineering perspective, the results highlight the importance of accounting for ambient flow direction, confinement, and buoyancy in the design of marine outfalls. Counter-flow conditions combined with weak confinement can enhance mixing through instability-driven mechanisms, whereas strong confinement may suppress these effects and delay dilution.

CRediT authorship contribution statement

Sina Tahmooresi: Writing – review & editing, Writing – original draft, Visualization, Validation, Software, Methodology, Investigation, Formal analysis. **Abdolmajid Mohammadian:** Writing – review & editing, Supervision, Resources, Methodology. **Ioan Nistor:** Writing – review & editing, Supervision, Resources. **Simone Ferrari:** Writing – review & editing, Supervision, Methodology.

Declaration of competing interest

The authors declare that they have no known competing financial interests or personal relationships that could have appeared to influence the work reported in this paper.

Acknowledgments

This research was primarily supported by the International Experience Bursary for graduate students at the University of Ottawa. The authors also acknowledge the institutional support provided by the University of Cagliari, where the experimental work was conducted. The authors gratefully acknowledge the assistance of Nicola Deiana and Robert Stuart, undergraduate students at the University of Cagliari, for their support during the experimental campaign. The numerical simulations presented in this work were made possible through the

Table 5
Mesh configurations (M1–M3) used in the mesh-independence analysis for $U_rF = 1.25$ and $H_0/D = 2.5,\ 5,\ 10$. The region of interest (ROI) is defined as $-10 < x^* < 40$, $-H_0/D < y^* < 10$, and $-10 < z^* < 10$.

Mesh	ROI Spacing (dx, dy, dz)	ROI Grading (x, y, z)	Outer Y,Z Grading
M1 (Medium)	$(D/4,\ D/4,\ D/4)$	$(1,\ 1,\ 1.025)$	1.15
M2 (Coarse)	$(D/2,\ D/4,\ D/4)$	$(1,\ 1,\ 1.025)$	1.15
M3 (Fine)	$dx = D/4$, $dy = \begin{cases} D/8, & -H_0/D < y/D \le 0, \\ D/4, & 0 < y/D < 10, \end{cases}$ $dz = D/4$	$(1,\ 1,\ 1)$	1.15

computational resources and support provided by the Digital Research Alliance of Canada. The research was also supported by the Natural Sciences and Engineering Research Council of Canada (NSERC).

Appendix A

A.1. Mesh independency study

Table 5 summarizes the three meshes (M1–M3) used in the mesh-independence analysis. The refinement strategies differ only within the region of interest (ROI), defined as $-10 < x^* < 40$, $-H_0/D < y^* < 10$, and $-10 < z^* < 10$, which encloses the near-field dynamics of the dense jet and the region where momentum, buoyancy, and recirculation interact most strongly (Fig. A.1). Mesh M1 represents the medium resolution and employs uniform spacing of $D/4$ in all three directions with a mild spanwise stretching (grading of 1.025 in the z direction). Mesh M2 is coarser in the streamwise direction ($dx = D/2$) while maintaining the same vertical and spanwise spacings as M1, resulting in reduced resolution primarily along the jet axis. Mesh M3 provides the finest resolution, incorporating an increased vertical refinement near the bottom wall ($dy = D/8$ for $-H_0/D < y/D \le 0$), where shear production and densimetric effects are most important, and uniform spacing above the jet centerline. Outside the ROI, all meshes use identical grading in the vertical and spanwise directions (grading factor 1.15). The streamwise mesh outside the ROI transitions smoothly from $D/2$ to $2D$. All three meshes were constructed to satisfy the requirement $y^+ < 10$–11 on solid boundaries, to be compatible with OpenFOAM wall function implementations for wall treatment in *nutLowReWallFunction*, *kLowReWallfunction*, and *omegaWallFunction*. Mesh-independence was evaluated for the most demanding condition, $U_rF = 1.25$, for all confinement ratios ($H_0/D = 2.5,\ 5,\ 10$) and for both co-flow and counter-flow configurations.

Fig. A.2 present sample results from the three investigated meshes for centerline trajectory y^*, the concentration decay C_m/C_0, and the wall normal resolution y^+ for cases with $H_0/D = 10.0$ and 2.5. The median mesh $M1$ and the fine mesh $M3$ show very similar performance in predicting the trajectory. For the concentration decay, only marginal difference are observed among the meshes for the cases shown. All three meshes maintain $y^+ < 10 - 11$. Considering these results across both flow types and all confinement ratios, and for the current Froude number $U_rF = 1.25$, the medium mesh $M1$ was selected for the remaining 48 numerical scenarios.

A.2. Frequency domain analysis of the centerline displacement

To quantify the dominant oscillation frequencies of the jet flapping motion, the temporal variation of the jet centerline position $y_c'(t)$ was analyzed in the frequency domain. The power spectral density (PSD) of the signal was computed using the fast Fourier transform (FFT), expressed as

$$PSD(f) = \frac{1}{N f_s} |\Sigma_{n=0}^{N-1} y_c'(n) e^{-i2\pi f_n/f_s}|^2 \tag{36}$$

where f is the frequency in Hertz, f_s is the sampling frequency, and N is the number of the temporal samples. The PSD represents the distribution of the variance (energy) of the signal as a function of frequency. PSDs were computed for the centerline displacement signals at selected non-dimensional streamwise stations x^*. To facilitate cross-section comparison within each case, spectra were normalized by their global peak:

$$\widetilde{PSD} = \frac{PSD(f)}{max(PSD(f))} \tag{37}$$

The interplay between confinement and counter-flow dynamics was further examined through spectral analysis of the centerline position time series, where jet mixing and evolution are commonly assessed. By applying FFT to the time-domain data of vertical displacements at multiple streamwise positions, the frequency content of the jet motion was extracted. The resulting power spectral density (PSD) quantifies how the variance (energy) of the signal is distributed over frequency. This offers insights into dominant oscillatory behaviors.

Fig. A.3 presents normalized PSDs for four selected cases with $H_0/D = 10$ and 2.5, under both co- and counter-flow conditions at $U_rF = 1.25$. In the counter-flow case with low confinement ($H_0/D = 10$), a dominant low-frequency peak emerges at approximately $f = 0.1$–0.3 Hz, particularly prominent from $x^* = 8$ to 16, indicating a quasi-periodic flapping behavior. The narrow bandwidth of this peak suggests a coherent instability mechanism, likely related to shear layer development. Notably, this corresponds with the location of maximum concentration decay observed in the average concentration field. The weak confinement in this case allows the shear layer to evolve relatively unimpeded.

Conversely, the counter-flow case with strong confinement ($H_0/D = 2.5$) exhibits a broader spectrum, with energy distributed across multiple low-frequency peaks ranging from $f = 0.2$ to 1.0 Hz. Here, confinement restricts vertical motion and amplifies interactions with the wall and background flow, dispersing the energy across a range of modes. This spectral signature is consistent with intermittent flapping and potential mode switching between wall-driven and shear layer-dominated dynamics.

In contrast, co-flow scenarios exhibit distinct spectral characteristics. At low confinement ($H_0/D = 10$), higher frequency peaks emerge, typically in the range of $f = 1.0$–1.5 Hz, often accompanied by multiple harmonics. These indicate convective instabilities associated with periodic vortex shedding or pairing events, rather than large-scale flapping. The co-flow case with higher confinement ($H_0/D = 2.5$) shows irregular harmonic amplitudes, suggesting disruption of coherent structures due to the proximity of the wall.

A.3. Frequency domain analysis of POD modes

To quantify the spectral behavior of POD temporal coefficients $a_k(t)$, their PSD were computed using FFT. From the PSDs, the following metrics were extracted:

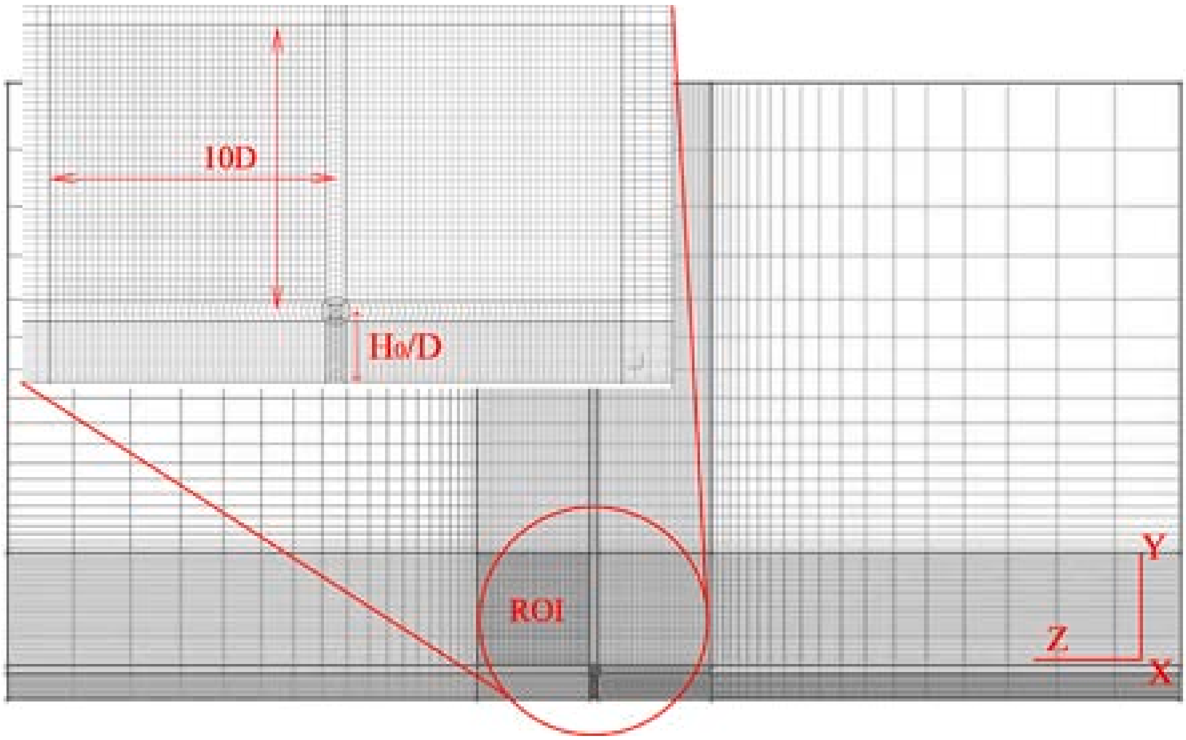

Fig. A.1. Mesh overview in $y-z$ plane. The three-dimensional mesh grids were built by extruding the $y-z$ plane in backward ($-200D$) and forward ($+200D$) directions with various progression rates.

(i) Band energy fraction. Let $f_{\rm dom}$ be the dominant frequency corresponding to the maximum of $P_k(f)$. The *band energy fraction* represents the fraction of the total spectral energy that is contained within a narrow frequency band Δf centered at $f_{\rm dom}$:

$$\eta_{\rm band} = \frac{\int_{f_{\rm dom}-\Delta f}^{f_{\rm dom}+\Delta f} P_k(f)\,{\rm d}f}{\int_0^{f_{\max}} P_k(f)\,{\rm d}f}. \tag{38}$$

(Ii) Quality factor. The *quality factor* (or sharpness of the spectral peak) quantifies the coherence of the dominant oscillation. The full width at half maximum (FWHM) of the dominant peak is defined as the frequency interval between f_L and f_R such that $P_k(f_L) = P_k(f_R) = \frac{1}{2}P_k(f_{\rm dom})$. The quality factor is then given by

$$Q_{\rm FWHM} = \frac{f_{\rm dom}}{f_R - f_L}. \tag{39}$$

(Iii) Prominence. The *prominence* describes how strongly the dominant spectral peak stands out relative to the surrounding broadband background. Let $P_{\rm pk} = P_k(f_{\rm dom})$ denote the amplitude of the dominant peak, and let $P_{\rm bg}$ represent a background level, defined here as the median spectral power outside the $\pm\Delta f$ neighborhood of $f_{\rm dom}$. The prominence is expressed as

$$\Pi = \frac{P_{\rm pk}}{P_{\rm bg}}. \tag{40}$$

From Fig. A.4 and Table 6, for the counter-flow case, Modes 1–2 exhibit nearly identical frequencies ($f_{\rm dom} \approx 0.14$ Hz) with very high band energy fractions (0.96 and 0.93) and moderate sharpness ($Q \approx 5.5$ and 3.7). These two modes form a pair representing the global flapping motion of the jet column. In contrast, in the co-flow case, the first two modes show much lower dominant frequencies ($f_{\rm dom} \approx 0.012$–0.40 Hz) with smaller Q values ($Q \approx 1$–16) and reduced band energy fractions (0.78 and 0.59), indicating that the co-flow redistributes energy toward broader, less coherent motions.

Mode 3 in the counter-flow case shows a higher-frequency narrowband component ($f_{\rm dom} \approx 0.24$ Hz, $Q \approx 9.5$, band fraction 0.66), characteristic of coherent shear layer oscillations. The co-flow counterpart exhibits a lower $f_{\rm dom} \approx 0.025$ Hz and a broad peak ($Q \approx 1.0$, band fraction 0.71), suggesting slow modulations or residual unsteady motion rather than a distinct convective tone. Mode 4 in both cases lies near $f_{\rm dom} \approx 0.01$–0.11 Hz, with $Q \approx 4$–1 and comparable energy fractions (0.62–0.50), representing low-frequency meandering or amplitude modulation of the main structure. Mode 5 remains broadband and weakly coherent in both flows ($f_{\rm dom} \approx 0.05$ Hz, $Q \approx 1.3$–0.5), capturing slow drift or long-time intermittency. Finally, Mode 6 in the counter-flow exhibits a higher-frequency narrowband response ($f_{\rm dom} \approx 0.36$ Hz, $Q \approx 9.7$, band 0.46), associated with organized shear layer activity or vortex pairing, whereas in the co-flow it shifts to $f_{\rm dom} \approx 0.86$ Hz with a very high $Q \approx 34.5$, implying enhanced small-scale periodicity induced by the stabilizing ambient flow.

Higher-order modes further highlight differences between the two flow regimes. In the counter-flow, intermediate modes exhibit narrowband higher-frequency components linked to shear layer instabilities. Meanwhile, in the co-flow case, these modes become more dispersed, dominated by weaker, broadband features, or in some instances, shifted to even higher frequencies associated with small-scale periodic behavior.

It can be concluded that the counter-flow configuration concentrates most of its energy in the low-frequency, large-scale flapping doublet, while the co-flow condition weakens these global oscillations and promotes higher-frequency, spatially localized shear layer dynamics with sharper spectral signatures (see Table 7).

Appendix B. Supplementary data

Supplementary material related to this article can be found online at https://doi.org/10.1016/j.ijheatmasstransfer.2026.129203.

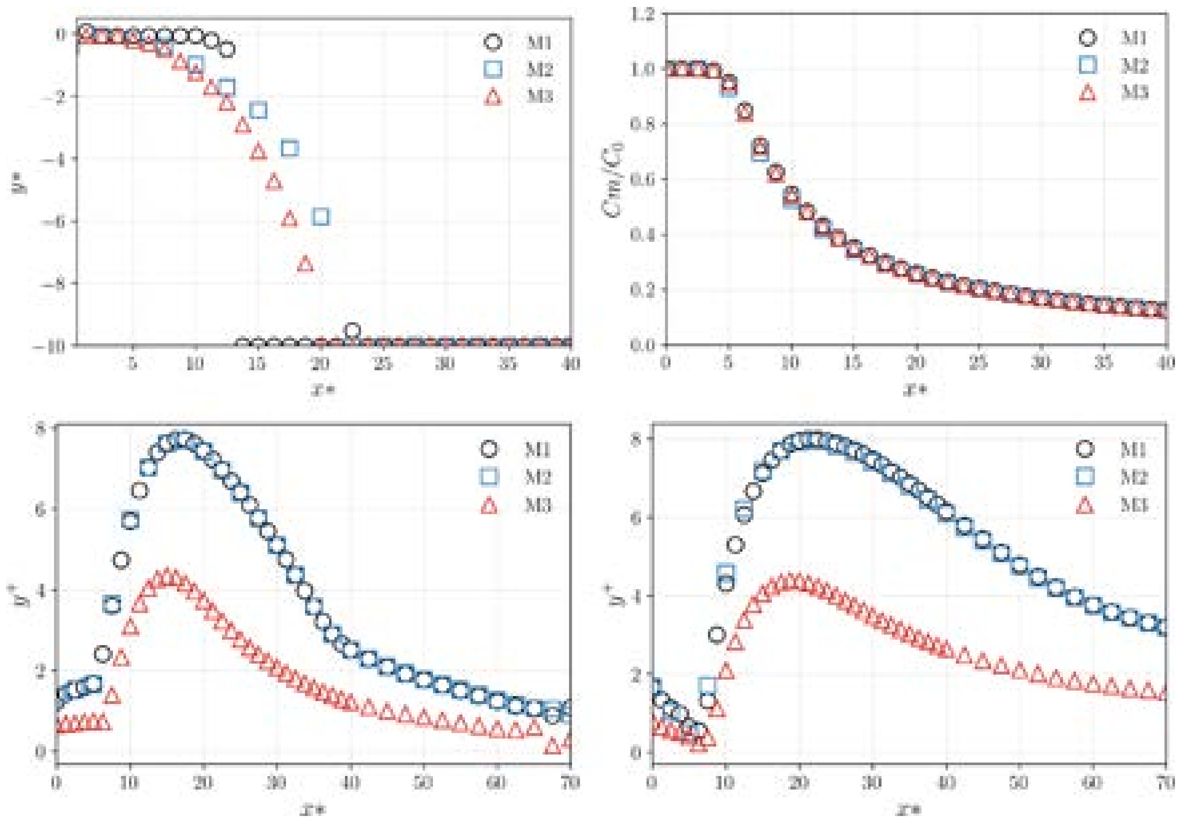

Fig. A.2. Mesh performance across three meshes $M1 - M3$. Top-left: trajectory for $H_0/D = 10$ in counter-flow; Top-right: Concentration decay for $H_0/D = 10$ in co-flow; Bottom-left: y^+ for $H_0/D = 2.5$ in counter-flow; Bottom-right: y^+ for $H_0/D = 2.5$ in co-flow.

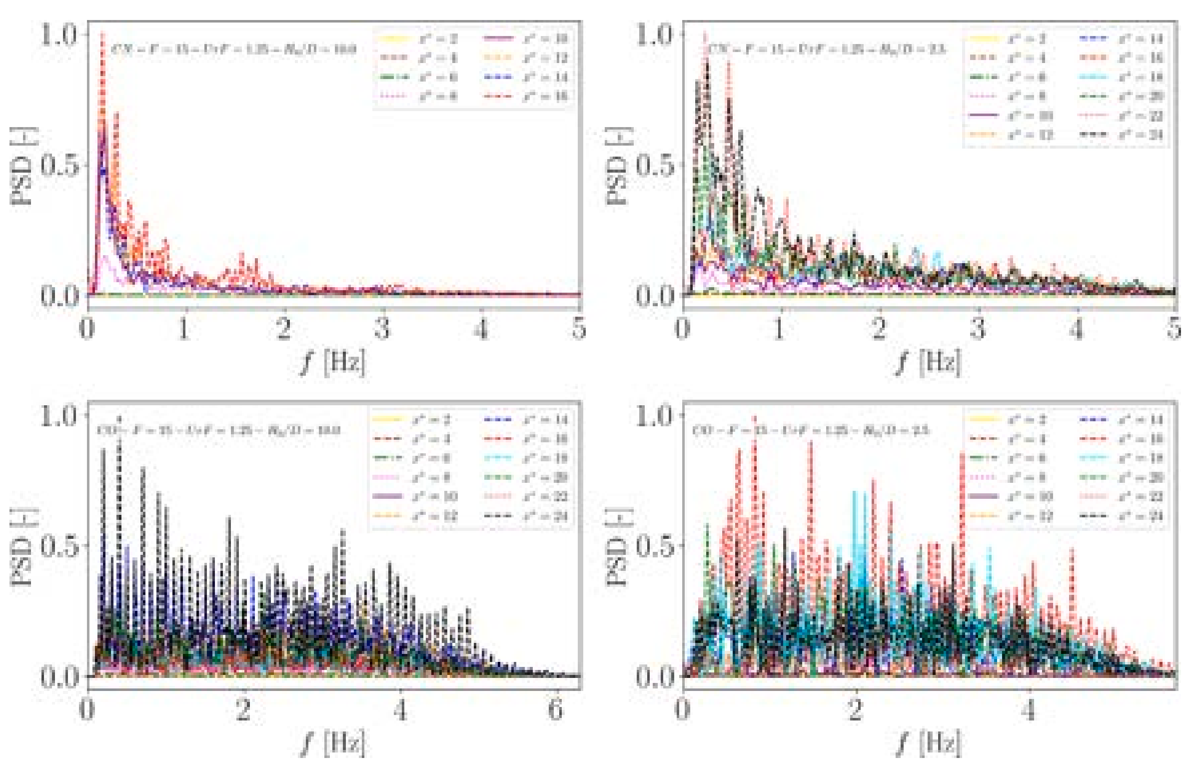

Fig. A.3. Power spectrum density (PSD) of the centerline position fluctuations for counter-flow (top) and co-flow (bottom) scenarios.

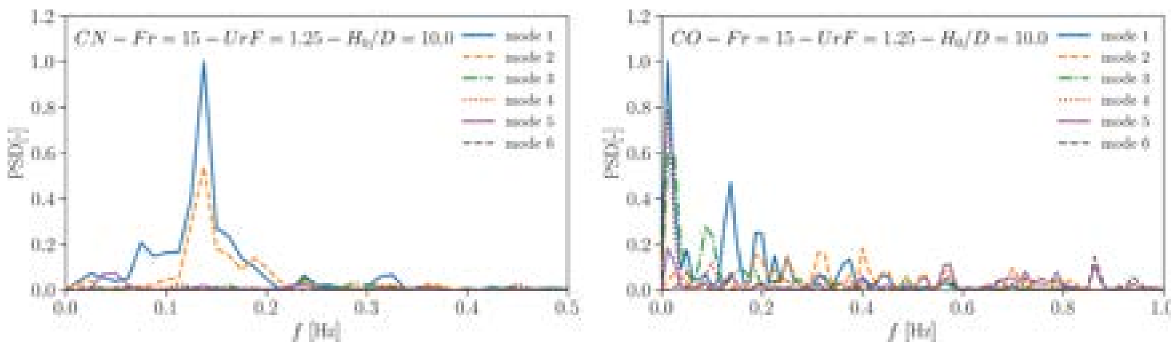

Fig. A.4. PSD analysis of the first six modes in counter flow (left) and co-flow (right) scenarios with $U_rF = 1.25$, $H_0/D = 10.0$, $F = 15$.

Table 6
Counter-flow: POD spectral metrics for modes 1–50 ($F = 15 - U_rF = 1.25 - H_0/D = 10$).

Mode	f_{dom} [Hz]	Band energy fraction	Q_{FWHM}	Prominence
1	0.14×10^0	0.96×10^0	5.50×10^0	6.95×10^4
2	0.14×10^0	0.93×10^0	3.67×10^0	6.18×10^4
3	0.24×10^0	0.66×10^0	9.50×10^0	6.09×10^3
4	0.11×10^0	0.51×10^0	4.50×10^0	1.61×10^4
5	0.05×10^0	0.68×10^0	1.33×10^0	3.02×10^4
6	0.36×10^0	0.46×10^0	9.67×10^0	4.85×10^3
7	0.05×10^0	0.41×10^0	1.33×10^0	6.83×10^3
8	0.04×10^0	0.68×10^0	1.50×10^0	1.31×10^4
9	0.65×10^0	0.31×10^0	17.33×10^0	9.65×10^2
10	0.41×10^0	0.28×10^0	16.50×10^0	1.56×10^3
11	0.24×10^0	0.37×10^0	6.33×10^0	1.96×10^3
12	0.04×10^0	0.21×10^0	1.00×10^0	1.01×10^3
13	0.24×10^0	0.39×10^0	4.75×10^0	2.03×10^3
14	0.25×10^0	0.38×10^0	10.00×10^0	7.61×10^2
15	0.25×10^0	0.29×10^0	6.67×10^0	4.62×10^2
16	0.07×10^0	0.22×10^0	2.00×10^0	4.72×10^2
17	0.19×10^0	0.36×10^0	5.00×10^0	7.61×10^2
18	0.25×10^0	0.20×10^0	10.00×10^0	8.29×10^1
19	0.32×10^0	0.35×10^0	13.00×10^0	1.09×10^3
20	0.70×10^0	0.25×10^0	28.00×10^0	1.04×10^3
21	0.52×10^0	0.24×10^0	10.50×10^0	2.10×10^2
22	0.17×10^0	0.33×10^0	4.67×10^0	2.33×10^2
23	0.22×10^0	0.25×10^0	4.50×10^0	7.54×10^1
24	0.11×10^0	0.26×10^0	4.50×10^0	2.35×10^2
25	0.26×10^0	0.22×10^0	7.00×10^0	9.06×10^1
26	0.02×10^0	0.16×10^0	1.00×10^0	1.11×10^2
27	0.51×10^0	0.25×10^0	20.50×10^0	3.19×10^2
28	0.01×10^0	0.21×10^0	1.00×10^0	1.75×10^2
29	0.17×10^0	0.31×10^0	2.80×10^0	2.28×10^2
30	0.19×10^0	0.27×10^0	7.50×10^0	1.66×10^2
31	0.25×10^0	0.23×10^0	6.67×10^0	5.05×10^1
32	0.29×10^0	0.21×10^0	7.67×10^0	1.12×10^2
33	0.67×10^0	0.16×10^0	7.71×10^0	4.87×10^1
34	0.30×10^0	0.13×10^0	8.00×10^0	3.87×10^1
35	0.09×10^0	0.18×10^0	1.75×10^0	9.55×10^1
36	0.36×10^0	0.29×10^0	9.67×10^0	2.21×10^2
37	0.01×10^0	0.09×10^0	1.00×10^0	5.93×10^1
38	0.56×10^0	0.17×10^0	22.50×10^0	2.58×10^2
39	0.37×10^0	0.23×10^0	10.00×10^0	1.24×10^2
40	0.02×10^0	0.12×10^0	1.00×10^0	6.46×10^1
41	0.01×10^0	0.17×10^0	1.00×10^0	1.63×10^2
42	0.70×10^0	0.14×10^0	28.00×10^0	5.41×10^1
43	0.97×10^0	0.13×10^0	39.00×10^0	6.29×10^1
44	0.06×10^0	0.16×10^0	0.71×10^0	1.47×10^2
45	0.36×10^0	0.22×10^0	9.67×10^0	6.06×10^1
46	0.07×10^0	0.25×10^0	2.00×10^0	1.79×10^2
47	1.26×10^0	0.13×10^0	50.50×10^0	8.90×10^1
48	0.55×10^0	0.18×10^0	22.00×10^0	6.30×10^1
49	0.01×10^0	0.12×10^0	0.50×10^0	4.55×10^1
50	0.27×10^0	0.14×10^0	11.00×10^0	6.69×10^1

Table 7
Co-flow: POD spectral metrics for modes 1–50 ($F = 15 - U_r F = 1.25 - H_0/D = 10$).

Mode	f_{dom} [Hz]	Band energy fraction	Q_{FWHM}	Prominence
1	0.01×10^0	0.78×10^0	1.00×10^0	1.55×10^4
2	0.40×10^0	0.59×10^0	16.00×10^0	2.78×10^3
3	0.02×10^0	0.71×10^0	1.00×10^0	1.11×10^3
4	0.01×10^0	0.62×10^0	1.00×10^0	1.93×10^3
5	0.01×10^0	0.25×10^0	0.50×10^0	4.97×10^3
6	0.86×10^0	0.42×10^0	34.50×10^0	7.75×10^3
7	2.10×10^0	0.24×10^0	33.60×10^0	9.79×10^2
8	2.34×10^0	0.23×10^0	46.75×10^0	1.56×10^3
9	0.94×10^0	0.25×10^0	25.00×10^0	1.62×10^3
10	4.05×10^0	0.14×10^0	162.00×10^0	1.76×10^2
11	2.46×10^0	0.11×10^0	49.25×10^0	1.70×10^2
12	1.51×10^0	0.16×10^0	40.33×10^0	5.59×10^2
13	0.31×10^0	0.29×10^0	8.33×10^0	2.09×10^3
14	0.32×10^0	0.23×10^0	8.67×10^0	4.51×10^2
15	2.46×10^0	0.17×10^0	65.67×10^0	1.45×10^2
16	2.67×10^0	0.13×10^0	71.33×10^0	8.41×10^1
17	1.80×10^0	0.08×10^0	48.00×10^0	2.64×10^1
18	1.50×10^0	0.15×10^0	40.00×10^0	9.72×10^1
19	0.24×10^0	0.27×10^0	4.75×10^0	2.11×10^2
20	0.32×10^0	0.15×10^0	5.20×10^0	1.11×10^2
21	6.82×10^0	0.06×10^0	182.00×10^0	1.76×10^1
22	6.82×10^0	0.07×10^0	182.00×10^0	1.79×10^1
23	1.49×10^0	0.14×10^0	23.80×10^0	7.08×10^1
24	1.32×10^0	0.04×10^0	35.33×10^0	1.52×10^1
25	4.50×10^0	0.09×10^0	120.00×10^0	2.52×10^1
26	1.49×10^0	0.12×10^0	39.67×10^0	5.00×10^1
27	0.26×10^0	0.16×10^0	10.50×10^0	9.73×10^1
28	0.35×10^0	0.16×10^0	9.33×10^0	1.58×10^2
29	1.51×10^0	0.04×10^0	60.50×10^0	8.48×10^0
30	0.05×10^0	0.03×10^0	1.33×10^0	1.12×10^1
31	4.37×10^0	0.06×10^0	175.00×10^0	2.12×10^1
32	4.37×10^0	0.07×10^0	175.00×10^0	2.78×10^1
33	0.81×10^0	0.13×10^0	32.50×10^0	4.37×10^1
34	0.06×10^0	0.07×10^0	1.67×10^0	3.51×10^1
35	2.96×10^0	0.06×10^0	79.00×10^0	1.65×10^1
36	1.51×10^0	0.11×10^0	60.50×10^0	6.63×10^1
37	1.50×10^0	0.05×10^0	60.00×10^0	1.38×10^1
38	8.42×10^0	0.04×10^0	224.67×10^0	1.46×10^1
39	4.37×10^0	0.05×10^0	116.67×10^0	1.56×10^1
40	0.10×10^0	0.12×10^0	2.67×10^0	5.71×10^1
41	3.15×10^0	0.09×10^0	84.00×10^0	1.90×10^1
42	0.10×10^0	0.06×10^0	2.67×10^0	1.95×10^1
43	4.25×10^0	0.07×10^0	85.00×10^0	1.22×10^1
44	3.19×10^0	0.12×10^0	127.50×10^0	3.15×10^1
45	3.91×10^0	0.05×10^0	104.33×10^0	2.56×10^1
46	4.70×10^0	0.06×10^0	125.33×10^0	3.92×10^1
47	4.39×10^0	0.05×10^0	117.00×10^0	1.04×10^1
48	0.35×10^0	0.11×10^0	7.00×10^0	3.67×10^1
49	3.91×10^0	0.08×10^0	156.50×10^0	4.14×10^1
50	1.36×10^0	0.09×10^0	27.25×10^0	2.30×10^1

Data availability

The experimental data and the in-house developed post-processing code are available upon request from the corresponding author.

References

[1] Abhishek Mishra, Harekrishna Yadav, Lyazid Djenidi, Amit Agrawal, Experimental study of flow characteristics of an oblique impinging jet, Exp. Fluids 61 (2020) 1–16.
[2] Harekrishna Yadav, Amit Agrawal, Self-similar behavior of turbulent impinging jet based upon outer scaling and dynamics of secondary peak in heat transfer, Int. J. Heat Fluid Flow 72 (2018) 123–142.
[3] Adrian Wing-Keung Law, Herlina, An experimental study on turbulent circular wall jets, J. Hydraul. Eng. 128 (2) (2002) 161–174.
[4] M. Agelin-Chaab, M.F. Tachie, Characteristics and structure of turbulent 3D offset jets, Int. J. Heat Fluid Flow 32 (3) (2011) 608–620.
[5] Dongdong Shao, Adrian Wing-Keung Law, Mixing and boundary interactions of 30 and 45 inclined dense jets, Environ. Fluid Mech. 10 (2010) 521–553.
[6] Dongdong Shao, Adrian Wing-Keung Law, Turbulent mass and momentum transport of a circular offset dense jet, J. Turbul. (10) (2009) N40.
[7] M. Agelin Chaab, M.F. Tachie, Characteristics of turbulent three-dimensional offset jets, ASME J. Fluids Eng. 133 (5) (2011) 051203.
[8] Ali Assoudi, Sabra Habli, Nejla Mahjoub Saïd, Hervé Bournot, Georges Le Palec, Experimental and numerical study of an offset jet with different velocity and offset ratios, Eng. Appl. Comput. Fluid Mech. 9 (1) (2015) 490–512.
[9] A. Nasr, J.C.S. Lai, A turbulent plane offset jet with small offset ratio, Exp. Fluids 24 (1) (1998) 47–57.
[10] E. Vishnuvardhanarao, Manab Kumar Das, Conjugate heat transfer study of incompressible turbulent offset jet flows, Heat Mass Transf. 45 (9) (2009) 1141–1152.
[11] Zhiqiang Wang, Yingjie Hu, Xingxing Cheng, Ming Liu, Chunyuan Ma, Influence of offset angle of mid-secondary air nozzles on gas-particle flow characteristics in a furnace, Rsc Adv. 8 (32) (2018) 17764–17772.
[12] Xin Li, Maolin Zhou, Jianmin Zhang, Weilin Xu, Numerical study of the velocity decay of offset jet in a narrow and deep pool, Water 11 (1) (2018) 59.
[13] Fatemeh Hakimi, Babak Khorsandi, Dynamics of round turbulent offset jets in quiescent and coflowing environments, Phys. Fluids 36 (10) (2024).
[14] Hessam Tofighian, Abdolreza Aghajanpour, Ozeair Abessi, Mohammadmehdi Ramezani, Simulation of inclined dense jets in stagnant environments: an LES and experimental study, Environ. Fluid Mech. 22 (5) (2022) 1161–1185.
[15] Shayan Habibi, Amin Azadi, Bahar Firoozabadi, Identification of turbulent structures of inclined negatively buoyant jets with bed effects, Int. J. Heat Mass Transfer 208 (2023) 124040.
[16] Niki Soleimani Amiri, Ali Sheykh Bahai, Ozeair Abessi, Ali Ali Rahmani Firoozjaee, Numerical and experimental analysis of positively buoyant discharge through inclined nozzles, Int. J. Coast. Offshore Environ. Eng. (Ijcoe) (2024) e201148.
[17] Shiva Ghayoor, Mehdi Hamidi, Ozeair Abessi, Investigating discrepancies between jet and plume in mean and turbulent flow of 45o inclined dense jets, Ocean Eng. 293 (2024) 116569.
[18] Mahshid Goodarzi, Seyed Mostafa Siadatmousavi, Ebrahim Jabbari, Numerical investigation of bed slope and proximity effects on the dynamics of inclined dense jets, Environ. Fluid Mech. 26 (2) (2026) 18.
[19] Xinyun Wang, Abdolmajid Mohammadian, Simone Ferrari, Philip J.W. Roberts, Experimental investigation of the influence of a sloped bottom on the behavior of inclined dense jets, Environ. Process. 13 (1) (2026) 10.

[20] Dongdong Shao, Adrian Wing-Keung Law, Boundary impingement and attachment of horizontal offset dense jets, J. Hydro-Environ. Res. 5 (1) (2011) 15–24.
[21] JoséL Pérez Talavera, JoséJ Quesada Ruiz, Identification of the mixing processes in brine discharges carried out in Barranco del Toro Beach, south of Gran Canaria (Canary Islands), Desalination 139 (1–3) (2001) 277–286.
[22] Abdolmajid Mohammadian, Hossein Kheirkhah Gildeh, Ioan Nistor, CFD modeling of effluent discharges: A review of past numerical studies, Water 12 (3) (2020) 856.
[23] K.W. Choi, Chris C.K. Lai, Joseph H.W. Lee, Mixing in the intermediate field of dense jets in cross currents, J. Hydraul. Eng. 142 (1) (2016) 04015041.
[24] Tanmoy Mondal, Nidhal Hnaien, Mariem Ajmi, Kouather Ghachem, Lioua Kolsi, CFD investigation of thermal characteristics for a dual jet with a parallel co-flow, ACS Omega 7 (32) (2022) 27864–27875.
[25] Guancheng Li, Lijing Cheng, Jiang Zhu, Kevin E. Trenberth, Michael E Mann, John P. Abraham, Increasing ocean stratification over the past half-century, Nat. Clim. Chang. 10 (12) (2020) 1116–1123.
[26] Marc Rovira, Klas Engvall, Christophe Duwig, Proper orthogonal decomposition analysis of the large-scale dynamics of a round turbulent jet in counterflow, Phys. Rev. Fluids 6 (1) (2021) 014701.
[27] Endam Gungor, Philip J.W. Roberts, Experimental studies on vertical dense jets in a flowing current, J. Hydraul. Eng. 135 (11) (2009) 935–948.
[28] Mostafa Taherian, Abdolmajid Mohammadian, Buoyant jets in cross-flows: review, developments, and applications, J. Mar. Sci. Eng. 9 (1) (2021) 61.
[29] S.A.R. Saeidi Hosseini, Mostafa Taherian, Abdolmajid Mohammadian, Simone Ferrari, Philip J.W. Roberts, Mixing behavior of multiport diffusers with non-uniform port orientation, Desalination 567 (2023) 116962.
[30] Donald E. Barrick, M.W. Evans, B.L. Weber, Ocean Surface Currents Mapped by Radar: Mobile coastal units can map variable surface currents in real time to 70 kilometers, using ocean wave scatter, Science 198 (4313) (1977) 138–144.
[31] Qingwen Mao, Ping Shi, Kedong Yin, Jianping Gan, Yiquan Qi, Tides and tidal currents in the Pearl River Estuary, Cont. Shelf Res. 24 (16) (2004) 1797–1808.
[32] Michele Mossa, Peter A. Davies, Some aspects of turbulent mixing of jets in the marine environment, Water 10 (4) (2018) 522.
[33] Isabel Iglesias, Paulo Avilez-Valente, Ana Bio, Luísa Bastos, Modelling the main hydrodynamic patterns in shallow water estuaries: The Minho case study, Water 11 (5) (2019) 1040.
[34] Yanan Chen, Zhiguo He, Yingzhong Lou, Han Zhang, Rui Zhu, Samuel Ukpong Okon, Experimental study of horizontal heated buoyant jets in a linearly stratified ambience, Phys. Fluids 33 (4) (2021).
[35] Liam Milton-McGurk, Nicholas Williamson, S.W. Armfield, M.P. Kirkpatrick, K.M. Talluru, Entrainment and structure of negatively buoyant jets, J. Fluid Mech. 911 (2021) A21.
[36] C.J. Oliver, M.J. Davidson, R.I. Nokes, Removing the boundary influence on negatively buoyant jets, Environ. Fluid Mech. 13 (2013) 625–648.
[37] Sina Tahmooresi, Davoud Ahmadyar, Application of Reynolds flux modeling in CFD simulation of 45$f \circ f$ inclined negatively buoyant jets, Environ. Fluid Mech. 22 (1) (2022) 55–86.
[38] Danial Goodarzi, Abdolmajid Mohammadian, Saleh Rezaeiravesh, Numerical simulation of desalination brine discharges: Effects of inlet boundary conditions, Desalination (2025) 119389.
[39] H.C. Burridge, G.R. Hunt, Entrainment by turbulent fountains, J. Fluid Mech. 790 (2016) 407–418.
[40] C. Bourque, B.G. Newman, Reattachment of a two-dimensional, incompressible jet to an adjacent flat plate, Aeronaut. Q. 11 (3) (1960) 201–232.
[41] T.S. Lund, Augmented thrust and mass flow associated with two-dimensional jet reattachment, AIAA J. 24 (12) (1986) 1964–1970.
[42] Nallamuthu Rajaratnam, Kanakatti Subramanya, Plane turbulent reattached wall jets, J. Hydraul. Div. 94 (1) (1968) 95–112.
[43] R.A. Sawyer, The flow due to a two-dimensional jet issuing parallel to a flat plate, J. Fluid Mech. 9 (4) (1960) 543–559.
[44] R.A. Sawyer, Two-dimensional reattaching jet flows including the effects of curvature on entrainment, J. Fluid Mech. 17 (4) (1963) 481–498.
[45] A. Nasr, J.C.S. Lai, Comparison of flow characteristics in the near field of two parallel plane jets and an offset plane jet, Phys. Fluids 9 (10) (1997) 2919–2931.
[46] Angelos N. Findikakis, Adrian W.K. Law, Marine tailings disposal simulation, J. Hydraul. Eng. 124 (4) (1998) 370–383.
[47] J.R.R. Pelfrey, J.A. Liburdy, Mean flow characteristics of a turbulent offset jet, 1986.
[48] Heung Bok Song, Soon Hyun Yoon, Dae Hee Lee, Flow and heat transfer characteristics of a two-dimensional oblique wall attaching offset jet, Int. J. Heat Mass Transfer 43 (13) (2000) 2395–2404.
[49] E. Vishnuvardhanarao, Manab Kumar Das, Computation of mean flow and thermal characteristics of incompressible turbulent offset jet flows, Numer. Heat Transf. Part A: Appl. 53 (8) (2007) 843–869.
[50] E. Vishnuvardhanarao, Manab Kumar Das, Study of the heat transfer characteristics in turbulent combined wall and offset jet flows, Int. J. Therm. Sci. 48 (10) (2009) 1949–1959.
[51] M.R. Davis, H. Winarto, Jet diffusion from a circular nozzle above a solid plane, J. Fluid Mech. 101 (1) (1980) 201–221.
[52] M. Agelin-Chaab, M.F. Tachie, Characteristics of turbulent three-dimensional offset jets, 2011.
[53] G. Padmanabham, B.H. Lakshmana Gowda, Mean and turbulence characteristics of a class of three-dimensional wall jets—Part 1: Mean flow characteristics, 1991.
[54] J.J. Sharp, B.D. Vyas, Froude, The buoyant wall jet., Proc. Inst. Civ. Eng. 63 (3) (1977) 593–611.
[55] Rodney J. Sobey, Archie J. Johnston, Richard D. Keane, Horizontal round buoyant jet in shallow water, J. Hydraul. Eng. 114 (8) (1988) 910–929.
[56] A.J. Johnston, R.E. Volker, Round buoyant jet entering shallow water, J. Hydraul. Res. 31 (1) (1993) 121–138.
[57] A.J. Johnston, C.R. Phillips, R.E. Volker, Modeling horizontal round buoyant jets in shallow water, J. Hydraul. Eng. 120 (1) (1994) 41–59.
[58] M. Knudsen, I.R. Wood, The interaction between a boundary and a horizontal buoyant jet, J. Hydraul. Res. 28 (3) (1990) 375–385.
[59] Godwin F.K. Tay, Mohammad S. Rahman, Mark F. Tachie, Characteristics of a horizontal square jet interacting with the free surface, Phys. Rev. Fluids 2 (6) (2017) 064607.
[60] J. Adjetey, K. Fukuda, R. Balachandar, Effects of axisymmetric confinement on vortical structures emanating from round turbulent jets, Phys. Fluids 36 (9) (2024).
[61] Dongdong Shao, Dingyong Huang, Baoxin Jiang, Adrian Wing-Keung Law, Flow patterns and mixing characteristics of horizontal buoyant jets at low and moderate Reynolds numbers, Int. J. Heat Mass Transfer 105 (2017) 831–846.
[62] Duo Xu, Jun Chen, Experimental study of stratified jet by simultaneous measurements of velocity and density fields, Exp. Fluids 53 (2012) 145–162.
[63] Duo Xu, Jun Chen, Experimental study of sub-grid scale physics in stratified flows, in: Fluids Engineering Division Summer Meeting, vol. 55560, American Society of Mechanical Engineers, 2013, V01CT28A002.
[64] Duo Xu, Jun Chen, Experimental study of mixing and entrainment in a horizontal turbulent stratified jet, in: Fluids Engineering Division Summer Meeting, vol. 46247, American Society of Mechanical Engineers, 2014, V01DT26A003.
[65] Duo Xu, Jun Chen, Subgrid-scale dynamics and model test in a turbulent stratified jet with coexistence of stable and unstable stratification, J. Turbul. 17 (5) (2016) 443–470.
[66] Sina Tahmooresi, Danial Goodarzi, Abdolmajid Mohammadian, Ioan Nistor, LIF measurement of turbulent horizontal dense jets in stagnant ambient, Int. J. Heat Mass Transfer 244 (2025) 126867.
[67] R.A. Antonia, Robert William Bilger, An experimental investigation of an axisymmetric jet in a co-flowing air stream, J. Fluid Mech. 61 (4) (1973) 805–822.
[68] D.J. Smith, T. Hughes, Some measurements in a turbulent circular jet in the presence of a co-flowing free stream, Aeronaut. Q. 28 (3) (1977) 185–196.
[69] T.B. Nickels, A.E. Perry, An experimental and theoretical study of the turbulent coflowing jet, J. Fluid Mech. 309 (1996) 157–182.
[70] M.J. Davidson, H.J. Wang, Strongly advected jet in a coflow, J. Hydraul. Eng. 128 (8) (2002) 742–752.
[71] Paul C.K. Chu, Joseph H. Lee, Vincent H. Chu, Spreading of turbulent round jet in coflow, J. Hydraul. Eng. 125 (2) (1999) 193–204.
[72] Mingtao Jiang, Wei Chen, Adrian Wing-Keung Law, Mixing characteristics of 45° inclined duckbill dense jets in co-flowing currents, J. Hydro-Environ. Res. 36 (2021) 77–86.
[73] Mingtao Jiang, Adrian Wing-Keung Law, Shuai Zhang, Mixing behavior of 45 inclined dense jets in currents, J. Hydro-Environ. Res. 18 (2018) 37–48.
[74] Ali Galeshi, Ozeair Abessi, Mahdi Yousefifard, Ali Rahmani Firoozjaee, Inclined dense discharge in stagnant and wave environments: An experimental and numerical study, Ocean Eng. 278 (2023) 114045.
[75] Masoud Moeini, Babak Khorsandi, Laurent Mydlarski, Effect of coflow turbulence on the dynamics and mixing of a nonbuoyant turbulent jet, J. Hydraul. Eng. 147 (1) (2021) 04020088.
[76] Marc Rovira, Klas Engvall, Christophe Duwig, Review and numerical investigation of the mean flow features of a round turbulent jet in counterflow, Phys. Fluids 32 (4) (2020).
[77] M. Yoda, H.E. Fiedler, The round jet in a uniform counterflow: Flow visualization and mean concentration measurements, Exp. Fluids 21 (6) (1996) 427–436.
[78] Nallamuthu Rajaratnam, Turbulent Jets, vol. 5, Elsevier, 1976.
[79] C.H.C. Chan, Kit Ming Lam, Centerline velocity decay of a circular jet in a counterflowing stream, Phys. Fluids 10 (3) (1998) 637–644.
[80] O. König, H.E. Fiedler, The structure of round turbulent jets in counterflow: A flow visualization study, in: Advances in Turbulence 3: Proceedings of the Third European Turbulence Conference Stockholm, July 3–6, 1990, Springer, 1991, pp. 61–66.
[81] Kit Ming Lam, H.C. Chan, Investigation of turbulent jets issuing into a counterflowing stream using digital image processing, Exp. Fluids 18 (3) (1995) 210–212.
[82] Kit Ming Lam, C.H.C. Chan, Time-averaged mixing behavior of circular jet in counterflow: Velocity and concentration measurements, J. Hydraul. Eng. 128 (9) (2002) 861–865.

[83] Sayahnya Roy, Krishnendu Barman, Koustuv Debnath, Bijoy S. Mazumder, Quantification of turbulent structures in and around the boundary region of a turbulent round jet released into counter-flow, Measurement 171 (2021) 108758.

[84] Amani Amamou, Amira Amamou, Rim Ben Khalifa, Nejla Mahjoub Said, Numerical parametric study of turbulent counterflowing jets, Int. Commun. Heat Mass Transfer 155 (2024) 107526.

[85] S.F. Saghravani, A.S. Ramamurthy, Penetration length of confined counter flowing free jets, J. Hydraul. Eng. 136 (3) (2010) 179–182.

[86] M. Sivapragasam, M.D. Deshpande, S. Ramamurthy, Peter White, Turbulent jet in confined counterflow, Sadhana 39 (2014) 713–729.

[87] Zhi-wei Li, Yang Xiao, Hong-wu Tang, Mixing of a non-circular jet into a counterflow, China Ocean Eng. 29 (1) (2015) 91–104.

[88] S. Bernero, H.E. Fiedler, Application of particle image velocimetry and proper orthogonal decomposition to the study of a jet in a counterflow, Exp. Fluids 29 (Suppl 1) (2000) S274–S281.

[89] Christophe Duwig, Johan Revstedt, Large scale dynamics of a jet in a counter flow, in: Advances in Turbulence XII: Proceedings of the 12th EUROMECH European Turbulence Conference, September 7-10, 2009, Marburg, Germany, Springer, 2009, pp. 321–324.

[90] Albert B. Pincince, E. John List, Disposal of brine into an estuary, J. (Water Pollut. Control. Federation) (1973) 2335–2344.

[91] Jerry Lee Anderson, Frank L. Parker, Barry A. Benedict, Negatively Buoyant Jets in a Cross Flow, vol. 1, US Government Printing Office, 1973.

[92] W.R. Lindberg, Experiments on negatively buoyant jets, with and without cross-flow, in: Recent Research Advances in the Fluid Mechanics of Turbulent Jets and Plumes, Springer, 1994, pp. 131–145.

[93] Mitchell J. Baum, Badin Gibbes, Field-scale numerical modeling of a dense multiport diffuser outfall in crossflow, J. Hydraul. Eng. 146 (1) (2020) 05019006.

[94] Mitchell J. Baum, Badin Gibbes, Alistair Grinham, Simon Albert, Paul Fisher, Deb Gale, Near-field observations of an offshore multiport brine diffuser under various operating conditions, J. Hydraul. Eng. 144 (11) (2018) 05018007.

[95] K.M. Lam, W.Y. Lee, C.H. Chan, J.H. Lee, Global behaviors of a round buoyant jet in a counterflow, J. Hydraul. Eng. 132 (6) (2006) 589–604.

[96] Joseph Hun-wei Lee, Vincent H. Chu, Turbulent Jets and Plumes: A Lagrangian Approach, vol. 1, Springer Science & Business Media, 2003.

[97] Gerhard H. Jirka, Integral model for turbulent buoyant jets in unbounded stratified flows Part 2: Plane jet dynamics resulting from multiport diffuser jets, Environ. Fluid Mech. 6 (2006) 43–100.

[98] Raed Bashitialshaaer, Magnus Larson, Kenneth M. Persson, An experimental investigation on inclined negatively buoyant jets, Water 4 (3) (2012) 720–738.

[99] Chris C.K. Lai, Joseph H.W. Lee, Mixing of inclined dense jets in stationary ambient, J. Hydro-Environ. Res. 6 (1) (2012) 9–28.

[100] Ozeair Abessi, Philip J.W. Roberts, Multiport diffusers for dense discharges, J. Hydraul. Eng. 140 (8) (2014) 04014032.

[101] Nadeem Ahmad, Raouf E. Baddour, Minimum return dilution method to regulate discharge of brine from desalination plants, Can. J. Civ. Eng. 41 (5) (2014) 389–395.

[102] Damjan Blažeka, Julio Car, Nikša Krstulović, Concentration quantification of TiO2 nanoparticles synthesized by laser ablation of a Ti target in water, Materials 15 (9) (2022) 3146.

[103] Simone Ferrari, Giorgio Querzoli, Mixing and re-entrainment in a negatively buoyant jet, J. Hydraul. Res. 48 (5) (2010) 632–640.

[104] Mostafa Taherian, Seyed Ahmad Reza Saeidi Hosseini, Abdolmajid Mohammadian, Simone Ferrari, Philip J.W. Roberts, Laboratory study on inclined desalination discharges in perpendicular cross-flow, Desalination 583 (2024) 117719.

[105] Kemal Hanjalić, Brian Launder, Modelling Turbulence in Engineering and the Environment: Second-Moment Routes to Closure, Cambridge University Press, 2011.

[106] Michel O. Deville, Paul F. Fischer, Ernest H. Mund, High-Order Methods for Incompressible Fluid Flow, vol. 9, Cambridge University Press, 2002.

[107] Florian R. Menter, Two-equation eddy-viscosity turbulence models for engineering applications, AIAA J. 32 (8) (1994) 1598–1605.

[108] David C. Wilcox, Reassessment of the scale-determining equation for advanced turbulence models, AIAA J. 26 (11) (1988) 1299–1310.

[109] Brian Edward Launder, Dudley Brian Spalding, The numerical computation of turbulent flows, in: Numerical Prediction of Flow, Heat Transfer, Turbulence and Combustion, Elsevier, 1983, pp. 96–116.

[110] Thomas Bonometti, S. Balachandar, Effect of Schmidt number on the structure and propagation of density currents, Theor. Comput. Fluid Dyn. 22 (5) (2008) 341–361.

[111] Carlo Gualtieri, Athanasios Angeloudis, Fabian Bombardelli, Sanjeev Jha, Thorsten Stoesser, On the values for the turbulent Schmidt number in environmental flows, Fluids 2 (2) (2017) 17.

[112] Nian-Sheng Cheng, Power-law index for velocity profiles in open channel flows, Adv. Water Resour. 30 (8) (2007) 1775–1784.

[113] Philip J.W. Roberts, Adrian Ferrier, Greg Daviero, Mixing in inclined dense jets, J. Hydraul. Eng. 123 (8) (1997) 693–699.

[114] Hugo B. Fischer, Mixing in Inland and Coastal Waters, Academic Press, 1979.

[115] Philip J.W. Roberts, Dispersion of buoyant waste water discharged from outfall diffusers of finite length, 1977.

[116] S. Beltaos, N. Rajaratnam, Circular turbulent jet in an opposing infinite stream, 1973.

[117] Hiroyuki Tsunoda, Jun-Ichi Takei, Statistical characteristics of the cross-sectional concentration field in a round counter jet, J. Fluid Sci. Technol. 1 (2) (2006) 105–113.

[118] Stephen B. Pope, Turbulent Flows, Cambridge University Press, 2000.

[119] T. Watanabe, Y. Sakai, K. Nagata, Y. Ito, T. Hayase, Turbulent mixing of passive scalar near turbulent and non-turbulent interface in mixing layers, Phys. Fluids 27 (8) (2015).

[120] Gal Berkooz, Philip Holmes, John L. Lumley, The proper orthogonal decomposition in the analysis of turbulent flows, Annu. Rev. Fluid Mech. 25 (1) (1993) 539–575.

[121] Lawrence Sirovich, Turbulence and the dynamics of coherent structures. I. Coherent structures, Quart. Appl. Math. 45 (3) (1987) 561–571.

[122] K.M. Lam, Application of POD analysis to concentration field of a jet flow, J. Hydro-Environ. Res. 7 (3) (2013) 174–181.

[123] Masaru Kiya, Kyuro Sasaki, Structure of a turbulent separation bubble, J. Fluid Mech. 137 (1983) 83–113.

[124] Wolfgang Rodi, Turbulence Models and Their Application in Hydraulics, Routledge, 2017.

[125] Michela Garau, Maria Grazia Badas, Simone Ferrari, Alessandro Seoni, Giorgio Querzoli, Turbulence and air exchange in a two-dimensional urban street canyon between gable roof buildings, Bound.-Layer Meteorol. 167 (1) (2018) 123–143.